ADVANCED ELECTRONIC MATERIALS
www.advelectronicmat.de

Modulation of Heavy Metal/Ferromagnetic Metal Interface for High-Performance Spintronic Devices

*Shouzhong Peng, Daoqian Zhu, Jiaqi Zhou, Boyu Zhang, Anni Cao, Mengxing Wang, Wenlong Cai, Kaihua Cao, and Weisheng Zhao**

Spintronic devices such as magnetic tunnel junctions and skyrmions have attracted considerable attention due to features such as nonvolatility, high scalability, low power, and high speed. Over the past few years, innovative materials and new structures in this field have resulted in the emergence of new phenomena and exciting device performance. It has been found that the heavy metal (HM)/ferromagnetic metal (FM) interface plays an essential role in spintronic devices. Spintronic device performance can be significantly enhanced through proper modulation of this interface. Recent progress in this blooming field is reviewed with specific emphasis on the HM/FM interface. Investigations into HM/FM-interface-related phenomena, including perpendicular magnetic anisotropy, tunnel magnetoresistance, magnetic damping, spin–orbit torque, and Dzyaloshinskii–Moriya interaction, are put into context. Guidelines for realizing high-performance spintronic devices are provided, and an outlook on their future research direction and potential applications is given.

1. Introduction

Since the discovery of the giant magnetoresistance effect, extensive efforts have been devoted to the development of spintronic devices and hence a lot of new phenomena and structures were found.[1,2] One of the most important devices is the magnetic tunnel junction (MTJ), which consists of a reference layer and a free layer separated by an insulating barrier layer. The magnetization of the reference layer is usually fixed, while that of the free layer is feasible to be switched by methods such as external magnetic field, spin-transfer torque (STT), and spin–orbit torque (SOT).[3–6] Due to the tunnel magnetoresistance (TMR) effect, an MTJ can exhibit low tunneling resistance and high tunneling resistance when the magnetizations in two ferromagnetic metal (FM) layers are in parallel configuration (PC) and antiparallel configuration (APC), respectively.[7] Consequently, MTJs can be used as memory cells in magnetic random-access memories (MRAMs). Magnetic skyrmion is another kind of emerging spintronic device.[8–10] It is expected to possess topologically protected stability, great scalability, and extremely low driving current density, promising to be employed in future magnetic memories and prospective integrated circuits.[11] Besides, utilizing magnetic domains as data carriers is also an attractive research direction in spintronics. The experimental demonstration of current-driven domain wall (DW) motion in magnetic nanowires shows the potential to build low-power and high-density racetrack memories.[12,13]

In early studies of spintronic devices, the magnetization of the FM layer lies in the film plane. A strong TMR effect can be realized in the in-plane magnetized MTJs (i-MTJs) with CoFeB/MgO/CoFeB structures.[14,15] However, these devices suffer from problems such as low switching efficiency and limited scalability. One of the breakthroughs is the discovery of interfacial perpendicular magnetic anisotropy (PMA) in the CoFeB/MgO/CoFeB structure, which possesses high TMR ratio, low magnetic damping, and relatively small STT switching current. Since then, plenty of endeavors have been put to optimize the CoFeB/MgO interface so as to improve performances.[16]

Further experiments demonstrate that, apart from the CoFeB/MgO interface, the heavy metal (HM) layer adjacent to the FM layer is also very important for device performances, as shown in **Figure 1**. For instance, by replacing the widely used HM material tantalum (Ta) with tungsten (W), both the interfacial PMA and the TMR ratio in the HM/CoFeB/MgO structure can be increased.[17,18] Moreover, the performance of the Ta/CoFeB/MgO structure deteriorates rapidly when the annealing temperature (T_a) exceeds 300 °C, while that of the W/CoFeB/MgO structure remains stable at annealing temperature up to 450 °C. The high thermal stability indicates that W-based structures are compatible with standard complementary metal–oxide semiconductor (CMOS) back-end-of-line processes, making W more attractive than Ta for practical applications. As for the magnetization switching, STT and SOT switching current can be reduced by decreasing magnetic damping constant and increasing spin Hall angle, respectively,

Dr. S. Peng, D. Zhu, J. Zhou, B. Zhang, A. Cao,
Dr. M. Wang, W. Cai, K. Cao, Prof. W. Zhao
Fert Beijing Institute
BDBC
School of Microelectronics
Beihang University
Beijing 100191, China
E-mail: weisheng.zhao@buaa.edu.cn
Dr. S. Peng, Prof. W. Zhao
Hefei Innovation Research Institute
Beihang University
Hefei 230013, China
The ORCID identification number(s) for the author(s) of this article can be found under https://doi.org/10.1002/aelm.201900134.

DOI: 10.1002/aelm.201900134

which is feasible by modulating the HM/FM interface. Besides, the creation and maintenance of skyrmions rely on the Dzyaloshinskii–Moriya interaction (DMI) effect, which is tunable by regulating the HM/FM interface. Consequently, not only the FM/insulator interface but also the HM/FM interface should be taken into consideration when the performances of spintronic devices are optimized.

In this review, we discuss recent developments of spintronic device performances through the modulation of the HM/FM interface. We begin by describing the effect of HM/FM interface on the PMA of several structures. Novel stacks for the free layer and reference layer are analyzed. Then experimental and theoretical investigations about the modulation of HM/FM interface for high TMR ratio are presented. Next, magnetic damping constant and SOT switching are discussed with emphasis on the low-power SOT switching. Finally, the investigations of DMI in different HM/FM systems are reviewed.

2. Modulation of HM/FM Interface for Strong PMA

Spin-transfer torque magnetic random-access memory (STT-MRAM) is becoming a kind of mainstream memory due to its nonvolatility, infinite endurance, low power, and high speed.[19–21] The core component in STT-MRAM is MTJ, which consists of two magnetic layers separated by a thin insulating layer. Conventional MTJs possess in-plane magnetic anisotropy (IMA) for the magnetic layers. However, problems such as poor scalability and low STT switching efficiency exist in these MTJs. Consequently, a lot of efforts have been put into the investigation of perpendicularly magnetized MTJs (p-MTJs).

2.1. PMA in Co-Based Multilayers

Perpendicularly magnetized palladium (Pd)/cobalt (Co) multilayer structures were investigated by Carcia et al. in 1985. The magnetic anisotropy at Pd/Co interfaces and strain in Co layers induce the PMA in this structure.[22] Platinum (Pt) in contact with Co can also generate interfacial PMA with the (111) texture.[23,24] Co/Pd (Pt) multilayers are then used as free layer and reference layer in p-MTJs. However, the low spin polarization results in a small TMR ratio,[25,26] while the relatively thick multilayers of Co/Pd (Pt) require a high threshold current for the magnetization reversal. In 2010, Yakushiji et al. achieved a high TMR ratio of 62% with the MgO-based p-MTJ consisting of ultrathin $[Co/Pt]_n$ and $[Co/Pd]_n$ multilayers adherent to CoFeB layer.[27] Co/Pt-based multilayers with strong PMA are also used as bottom reference layer in p-MTJs, where thermally robust p-MTJ with TMR ratio of 150% is achieved after 30 min annealing at 400 °C.[28] Perpendicularly magnetized synthetic antiferromagnetically (p-SAF) coupled reference structure with strong interlayer exchange coupling (IEC) was explored by Yakushiji et al., where two series of Co/Pt multilayers were separated by a ruthenium (Ru) layer.[29] The p-MTJ based on this p-SAF reference layer shows a TMR ratio of 110–150%. In 2017, they replaced the Ru layer with an iridium (Ir) layer, where a higher IEC energy density with a wider Ir layer thickness range is obtained. A high TMR ratio of 131% is maintained in these p-MTJs,[30] which indicates a more stable reference layer for p-MTJs.

Co/nickel (Ni) multilayers also show tunable PMA with high spin polarization[31] and low magnetic damping.[32] The origin of PMA in the Co/Ni multilayers is explained by the large magnetic anisotropy energy (MAE) arising from the interface between ultrathin Co and Ni layers, the number of valence electron that places the Fermi energy close to bands whose spin–orbit coupling (SOC) favors PMA,[33] and the magnetoelastic anisotropy due to strain.[34] Strong PMA was demonstrated in epitaxial Co/Ni multilayers grown on sapphire substrate.[35] In addition, magnetron sputtering was also employed to deposit Co/Ni multilayers.[36] PMA can be obtained for as-deposited samples when the Co/Ni multilayers are deposited on Pt buffer layer, while post annealing is needed for achieving PMA when

Shouzhong Peng is an assistant professor at Beihang University, Beijing, China. He received his B.S. degree in electronic and information engineering from Beihang University in 2013 and a Ph.D. degree in microelectronics and solid-state electronics from Beihang University in 2018. His research interests include spintronic devices, nanoscale physics and materials, nonvolatile memory, and first-principles calculations.

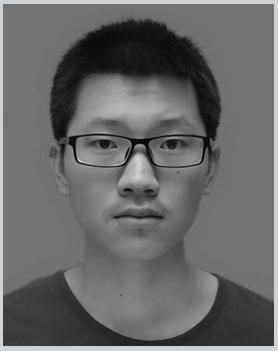

Daoqian Zhu received a B.S. degree in electronic and information engineering from Beihang University, Beijing, China, in 2017. He is currently pursuing a Ph.D. degree in microelectronics and solid-state electronics at Beihang University. His research interests include spin–orbit torque and magnetic skyrmions.

Jiaqi Zhou received a B.S. degree in electronic science and technology from Sichuan University in 2014. She is currently working toward a Ph.D. degree at the Fert Beijing Institute of Beihang University, Beijing, China. She is interested in the design of magnetic tunnel junctions and the optimization of their properties, in particular the tunneling–magnetoresistance ratio.

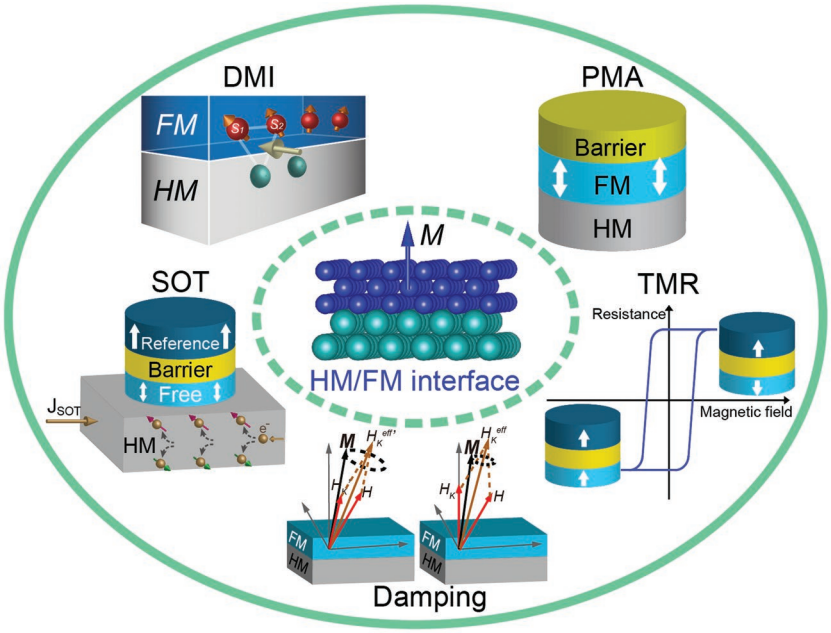

Figure 1. A schematic of the HM/FM interface (inner ellipse) and the related performance properties of spintronic devices (outer ellipse).

Co/Ni multilayers are deposited on MgO buffer layer. Due to the strong PMA, Co/Ni multilayers can serve as reference layer in p-MTJs, where a TMR ratio of 143% is obtained in Co/Ni-based p-MTJ stack with total thickness down to 10.6 nm.[37]

2.2. PMA in CoFeB/MgO/CoFeB Structures

In 2010, Ikeda et al. reported p-MTJs with the Ta/CoFeB/MgO/CoFeB/Ta structure, as shown in **Figure 2**.[38] This MTJ shows a TMR ratio of 124%, a thermal stability factor of 43, and a switching current of 49 μA at dimension of 40 nm diameter. The thermal stability factor Δ can be written as

$$\Delta = \frac{E_B}{k_B T} = \frac{KV}{k_B T} \tag{1}$$

where E_B is the energy barrier between the parallel and antiparallel states for the magnetization in the free layer and reference layer, k_B is the Boltzmann constant, T is the temperature, K and V are the anisotropy energy density and the volume of free layer, respectively. The anisotropy energy density ($K = M_s H_K/2$) of the CoFeB free layer can be approximately expressed as[38,39]

$$K = K_i / t_{CoFeB} + K_b - 2\pi M_s^2 \tag{2}$$

where M_s is the saturation magnetization, H_K is the anisotropy field, K_i is the interfacial magnetic anisotropy, K_b is the bulk magnetic anisotropy, t_{CoFeB} is the thickness of the CoFeB free layer. As shown in Figure 2b,c, the Ta/CoFeB/MgO structure exhibits IMA when the CoFeB layer is too thick (e.g., 2.0 nm), otherwise, it exhibits PMA when the CoFeB layer is thin enough (e.g., 1.3 nm). The K_i can be extracted from the intercept of Kt_{CoFeB} versus t_{CoFeB}, and the $K_b - 2\pi M_s^2$ can be obtained from the slope of it. As demonstrated in the inset of Figure 2c, the K_i of the Ta/CoFeB/MgO structure is 1.3 mJ m^{-2}, while the K_b is usually negligible for the CoFeB/MgO structures. Therefore, the PMA in this structure originates entirely from interfacial magnetic anisotropy.

First-principles calculations were performed to investigate the interfacial magnetic anisotropy at the Fe(Co)/MgO interface. In 2010, Niranjan et al. explored the magnetocrystalline anisotropy in the MgO/Fe/Cu structure.[40] It is found that this structure gives rise to PMA, which can be tuned by an electric field due to the redistributions of the Fe-3d orbital occupancy at the Fe/MgO interface. In addition, Yang et al. reported strong PMA at the Fe/MgO interface.[41] The origin of this interfacial PMA is attributed to the hybridization between Fe-3d and O-2p orbitals with SOC-induced splitting around the Fermi level. Moreover, the overoxidation or underoxidation at the interface will hinder the overlap between Fe-3d and O-2p orbitals, leading to a significant reduction of PMA, in agreement with experimental results. Further studies evaluated the contributions to PMA from each atomic layer of the Fe/MgO structure.[42] It is found that the PMA not only originates from the first interfacial Fe monolayer, but also propagates into several monolayers of the bulk Fe. These theoretical investigations elucidated the origin of PMA at the Fe/MgO interface.

2.3. PMA in HM/CoFeB/MgO Structures

In order to maintain data in MTJs for a long time (e.g., 10 years), it is essential to obtain strong PMA and high thermal stability. Moreover, when memory capacity increases, strong PMA is needed to guarantee low chip failure rate. As shown in **Figure 3**, for memories with capacity of 128 Gbit, a thermal stability factor of 75 is necessary to achieve data retention time of 10 years and chip failure rate of 10^{-4},[43–46] which requires the interfacial PMA of the free layer stronger than 4.7 mJ m^{-2} if MTJ size is smaller than 10 nm. Even though some applications, such as cache memory, demand much shorter retention time (e.g., 1 ms), an interfacial PMA value as high as 3.1 mJ m^{-2} is still needed. However, the typical interfacial PMA value for the widely used Ta/CoFeB/MgO structure is less than 2 mJ m^{-2}. Consequently, it is critical to enhance PMA in order to achieve large-capacity and high-density MRAMs.

Experiments showed that the HM/FM interface is vital for achieving strong PMA. In 2011, Worledge et al. deposited the HM/CoFeB/MgO structures with the Ta and Ru as the HM layer material.[47] After annealing, the Ta/CoFeB/MgO structure exhibits PMA when the CoFeB layer is thinner than 1.1 nm, whereas the Ru/CoFeB/MgO structure remains IMA. These results reveal that not only the CoFeB/MgO interface but also the HM/CoFeB interface is essential for PMA.

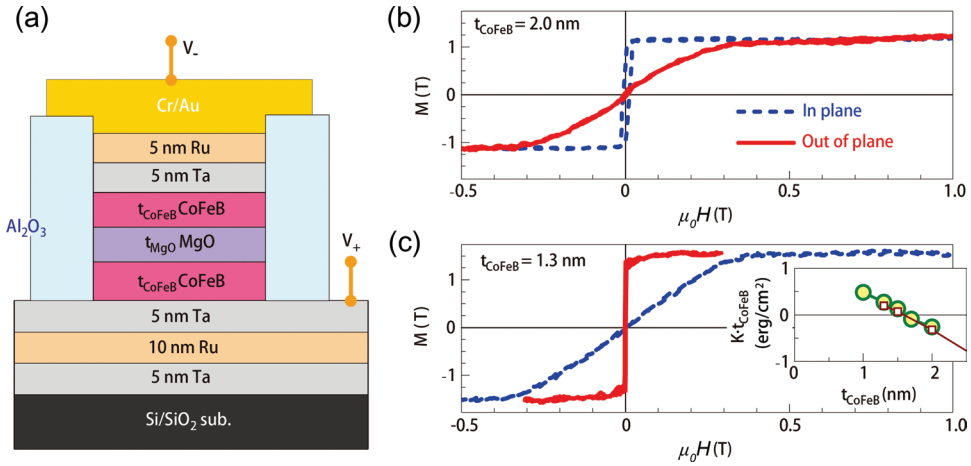

Figure 2. a) Schematic of MTJ structure. In-plane and out-of-plane magnetization curves for CoFeB/MgO structures with CoFeB thickness of b) t_{CoFeB}= 2.0 nm and c) t_{CoFeB}= 1.3 nm. Inset: t_{CoFeB} dependence of the product of anisotropy energy density (K) and t_{CoFeB}. The circles and squares show results obtained from magnetization and ferromagnetic resonance (FMR) measurements, respectively.[38] Reproduced with permission.[38] Copyright 2010, Nature Publishing Group.

Later on, PMA in the Ta/CoFeB/MgO structure was widely studied. For example, the influence of annealing temperature on the magnetic anisotropy was explored by several groups.[48–50] Annealing at a proper temperature will significantly enhance PMA. However, when the annealing temperature is higher than 350 °C, the Ta/CoFeB/MgO films cannot remain PMA due to the Ta diffusion, which hinders the integration with CMOS circuits because thermal treatment at about 400 °C is usually necessary for the back-end-of-line process. Cheng et al. investigated the effect of Ta thickness on the PMA of the MgO/CoFeB/Ta structure.[51] It is found that the structure with 1 nm Ta exhibits PMA both before and after annealing, whereas the one with 5 nm Ta changes from PMA to IMA after annealing at 300 °C for 1 h. Strong dependence of magnetic anisotropy on Ta thickness was also reported by several other groups.[52–57] These phenomena are attributed to Ta oxidation or diffusion of Ta into CoFeB layer during annealing. In 2012, Greer et al. studied the distribution of boron (B) in Ta/CoFeB/MgO structure with standing-wave hard X-ray photoemission.[58] It is observed that 19.5% of B diffuses into MgO layer and 23.5% of B migrates into Ta layer after annealing at 300 °C for 1 h. Wang et al. found that B atoms tend to diffuse into the Ta layer (MgO layer) for the underoxidized (overoxidized) Ta/CoFeB/MgO samples.[59] Moreover, the diffusion of B into HM layer contributes to the formation of Fe(Co)—O bonds, thus benefiting the enhancement of PMA.[56,60]

Further research found that strong PMA can also be obtained by replacing Ta with HM materials such as hafnium (Hf), niobium (Nb), and Ir. In 2012, Liu et al. investigated the magnetic properties of the Ta/CoFeB/MgO and Hf/CoFeB/MgO structures,[61] demonstrating that with the Ta replaced by Hf, the interfacial PMA increases from 1.7 to 2.3 mJ m^{-2}. Pai et al. obtained an interfacial PMA value of 1.9 mJ m^{-2} for the Hf/CoFeB/MgO structure, confirming again that Hf is a promising candidate for achieving strong PMA.[62] In 2014, Lee et al. systematically compared the magnetic behaviors in HM/CoFeB/MgO structures with HM materials of Ru, Ta, and Nb.[63] The Ta/CoFeB/MgO and Nb/CoFeB/MgO structures possess comparable interfacial PMA (≈2.2 mJ m^{-2}), whereas the Ru/CoFeB/MgO structure shows a much smaller one (0.68 mJ m^{-2}). Later in 2015, an interfacial PMA value of 1.9 mJ m^{-2} was acquired with the Ir/CoFeB/MgO structure.[64] Besides, HM materials such as titanium (Ti), Pt, Pd, vanadium (V) were also investigated.[65–70] All these studies show the importance of

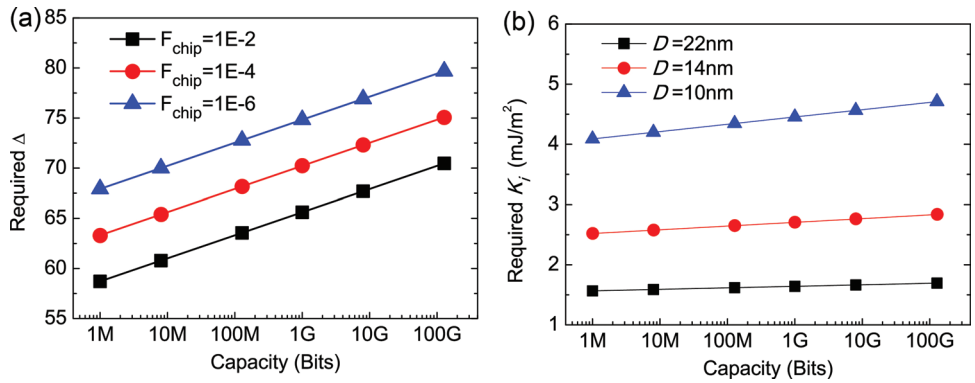

Figure 3. a) Required thermal stability factor Δ and b) interfacial magnetic anisotropy K_i as a function of capacity. Retention time of 10 years is assumed for (a) and chip failure rate of 10^{-4} is assumed for (b).[43] Reproduced with permission.[43] Copyright 2017, IEEE Publishing Group.

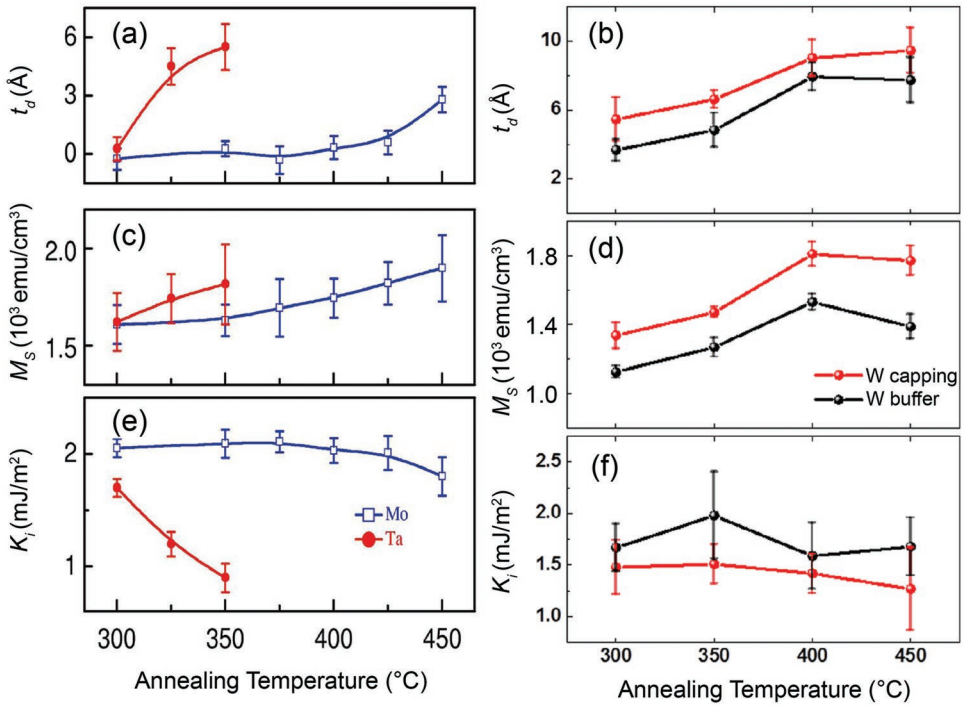

Figure 4. The annealing temperature dependence of a,b) magnetic dead layer t_d, c,d) saturation magnetization M_S, and e,f) interfacial magnetic anisotropy K_i for a,c,e) Ta/CoFeB/MgO, Mo/CoFeB/MgO structures[17] and b,d,f) W/CoFeB/MgO (W buffer), MgO/CoFeB/W (W capping) structures.[71] (a,c,e) Reproduced with permission.[17] Copyright 2015, Elsevier Publishing Group. (b,d,f) Reproduced with permission.[71] Copyright 2014, Nature Publishing Group.

the HM/FM interface and indicate the feasibility to strengthen PMA by choosing proper HM material.

Recent years have witnessed numerous efforts devoted to exploring proper material systems that can remain PMA after annealing at a high temperature. Liu et al. explored magnetic anisotropy in the molybdenum (Mo)/CoFeB/MgO structure at various annealing temperatures, as shown in **Figure 4**a.[71] It was demonstrated that this structure possesses 20% stronger PMA than that of the Ta/CoFeB/MgO. Moreover, while the PMA in the Ta/CoFeB/MgO structure decreases rapidly when the annealing temperature exceeds 300 °C, the Mo/CoFeB/MgO structure holds strong PMA after annealing at 425 °C. An et al. systematically investigated the magnetic anisotropy in W/CoFeB/MgO structure (see Figure 4b).[17] An interfacial PMA value of 1.98 mJ m^{-2} is obtained when the samples are annealed at 350 °C. More importantly, after annealing at 450 °C, the samples still exhibit interfacial PMA of 1.7 mJ m^{-2}. These features are mainly attributed to the B affinity of W and the strong PMA generated at the W/CoFeB interface. Similar results have been reported in several literatures.[70,72–77] These findings benefit the compatibility of p-MTJs with standard CMOS back-end-of-line processes and make W and Mo more attractive than Ta for practical applications.

Table 1 summarized the interfacial magnetic anisotropy of different HM/FM/MgO and MgO/FM/HM structures. After annealing at 300 °C, the interfacial magnetic anisotropy of the Ta/CoFeB/MgO structure varies from 1.3 to 2.2 mJ m^{-2}, while that of the Ru/CoFeB/MgO structure ranges from 0.5 to 0.68 mJ m^{-2}. Strong interfacial PMA can be obtained

Table 1. Interfacial magnetic anisotropy K_i of different HM/FM/MgO and MgO/FM/HM structures.

Heavy metal	Structure	T_a [°C]	K_i [mJ m^{-2}]	Ref.
Ta	Ta/CoFeB/MgO	300	1.3	[38]
Ta	Ta/CoFeB/MgO	240	1.8	[47]
Ru	Ru/CoFeB/MgO	240	0.5	[47]
Ta	Ta/CoFeB/MgO	300	1.5	[52]
Nitrogen doped Ta	Ta(N)/CoFeB/MgO	300	1.8	[52]
Ta	Ta/CoFeB/MgO	300	1.7	[61]
Hf	Hf/CoFeB/MgO	300	2.3	[61]
Hf	Hf/CoFeB/MgO	300	1.9	[62]
Ta	MgO/CoFeB/Ta	300	2.2	[63]
Ru	MgO/CoFeB/Ru	300	0.68	[63]
Nb	MgO/CoFeB/Nb	300	2.0	[63]
Ir	Ir/CoFeB/MgO	300	1.9	[64]
Pt	Pt/CoFeB/MgO	400	0.77	[68]
Ta	Ta/CoFeB/MgO	300	1.7	[71]
Mo	Mo/CoFeB/MgO	300	2.05	[71]
Mo	Mo/CoFeB/MgO	425	2.05	[71]
W	W/CoFeB/MgO	350	1.98	[17]
W	W/CoFeB/MgO	450	1.7	[17]
W	MgO/CoFeB/W	350	1.5	[17]
W	W/CoFeB/MgO	420	1.67	[72]

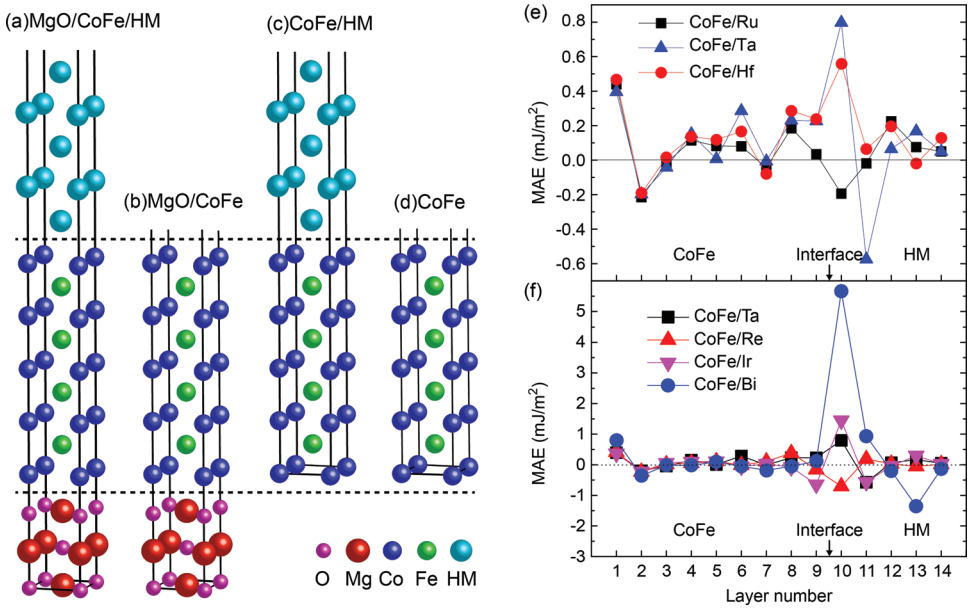

Figure 5. Schematics of atomic structures for a) MgO/CoFe/HM, b) MgO/CoFe, c) CoFe/HM, and d) CoFe thin films. e,f) Layer-resolved MAEs of different CoFe/HM structures. Nine CoFe monolayers (layer 1–9), five HM monolayers (layer 10–14), and a vacuum layer are included in the structures.[78,79] (a–e) Reproduced with permission.[78] Copyright 2015, Nature Publishing Group. (f) Reproduced with permission.[79] Copyright 2017, AIP Publishing Group.

with heavy metals of Ta, Hf, Nb, Ir, Mo, and W. Moreover, the Mo/CoFeB/MgO and W/CoFeB/MgO structures maintain strong PMA after annealing at high temperatures, making Mo and W promising in future magnetic memories and integrated circuits.

First-principles calculations were performed to elucidate the effect of HM layer on the PMA. Peng et al. investigated the MgO/CoFe/HM, MgO/CoFe, CoFe/HM, and CoFe structures, as shown in **Figure 5**a–d, with the HM layer of Ru, Ta, and Hf.[78] It is found that the MAE of the MgO/CoFe/HM structure originates from both the MgO/CoFe interface and the CoFe/HM interface, and that the CoFe/HM (HM = Ta and Hf) interface generates stronger PMA than the MgO/CoFe interface. Moreover, as shown in Figure 5e, different HM materials lead to quite different MAEs, which can be explained with the variations of SOC and orbital hybridizations at the CoFe/HM interface. These findings indicate that it is feasible to enhance PMA of the MgO/CoFe/HM structure by choosing proper HM material. In order to search for a structure with strong PMA, MgO/CoFe/HM systems with HM material of 5d metals Hf, Ta, rhenium (Re), osmium (Os), Ir, Pt, gold (Au), W and 6p metals thallium (Tl), plumbum (Pb), and bismuth (Bi) are explored, as plotted in Figure 5f.[79] Relatively strong PMA is observed in MgO/CoFe/HM structures with HM of Hf, Ta, Os, Ir, Pb, and W, consistent with experimental results.[17,47,61,64] Furthermore, by inserting a thin Fe layer at the CoFe/W interface, the PMA of the MgO/CoFe/W structure can be significantly strengthened.[80] Moreover, giant PMA (6.09 mJ m^{-2}) is predicted for the MgO/CoFe/Bi structure, which is about three times larger than the MAE (1.70 mJ m^{-2}) of the widely used MgO/CoFe/Ta structure. These works have paved new paths for the enhancement of PMA. More studies can be found in refs. [81–90].

2.4. PMA in MgO/CoFeB/HM/CoFeB/MgO Structures

In order to further strengthen PMA, double-interface structures (MgO/CoFeB/HM/CoFeB/MgO) are widely adopted as the free layer. In the MgO/CoFeB (1.6 nm)/Ta (0.4 nm)/CoFeB (1.0 nm)/MgO structure, two CoFeB layers can be switched simultaneously due to the strong IEC, thus can be used as a single free layer.[91] With two MgO/CoFeB interfaces and two CoFeB/Ta interfaces in this structure, the interfacial PMA is significantly enhanced. Consequently, the thermal stability is increased by a factor of 1.9 than the single-interface structure (MgO/CoFeB (1.6 nm)/Ta). In addition, even though the thermal stability is increased, the critical STT switching current of the double-interface structure remains comparable with the single-interface structure, which is attributed to the decrease of damping constant along with the increase of total CoFeB thickness. Further experiments find that as the MTJ diameter scales down from 70 to 11 nm, the critical STT switching current declines in the entire diameter range, while the thermal stability factor remains almost the same for diameters from 70 to 30 nm and starts to decrease at the diameter of 30 nm,[92–94] as shown in **Figure 6**a. Besides, the thermal stability factor of the MgO/CoFeB/Ta/CoFeB/MgO structure reduces to lower than 50 when the MTJ size shrinks down to 20 nm, which cannot meet the demand of large-capacity and high-density MRAMs.

In the MgO/CoFeB/HM/CoFeB/MgO structure, the HM spacer layer plays an essential role in determining the performances of the free layer. A number of efforts have been made to optimize the spacer layer so as to improve MTJ performances. In order to make two CoFeB layers switch simultaneously, a strong IEC is required. Cuchet et al. investigated the double-interface structures with spacer layer of Ru and Ta (0.2 nm)/Ru,[96] where the spacer material Ru is well-known to provide

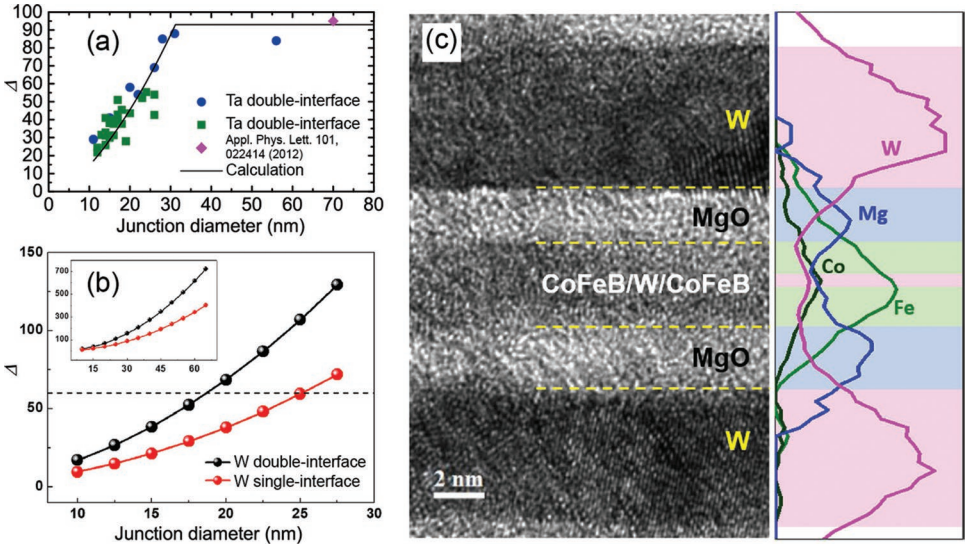

Figure 6. a,b) Thermal stability factor Δ as a function of junction diameter for a) Ta-based and b) W-based structures. c) Cross-sectional transmission electron microscopy (TEM) image and energy-dispersive X-ray spectroscopy (EDS) line profile of W (5 nm)/MgO (2 nm)/CoFeB (1.5 nm)/W (0.55 nm)/CoFeB (1.2 nm)/MgO (2 nm)/W (5 nm) structure. The sample was annealed at 350 °C.[92,95] (a) Reproduced with permission.[92] Copyright 2014, AIP Publishing Group. (b,c) Reproduced with permission.[95] Copyright 2015, Nature Publishing Group.

strong coupling.[97,98] Samples are annealed at 300 °C for 60 min in vacuum. Antiferromagnetic coupling is observed in the MgO/CoFeB/Ru/CoFeB/MgO structure when the Ru thickness ranges from 0.4 to 0.9 nm. The coupling strength reaches its maximum as Ru thickness is 0.55 nm and then decreases monotonously. When a Ta (0.2 nm) layer is inserted below the Ru spacer, the coupling strength dramatically reduces and reaches its maximum at Ru thickness of 0.5 nm. The largest antiferromagnetic coupling energies are estimated to be around 0.3 and 0.06 mJ m^{-2} for the spacer of Ru (0.6 nm) and Ta (0.2 nm)/Ru (0.5 nm), respectively. Besides, the MgO/CoFeB/Ru/CoFeB/MgO structure is found to be stable enough to act as reference layer in MTJs.

Double-interface structures with spacer layer of Mo were investigated by Zhang et al.[99] For the samples annealed at 300 °C, antiferromagnetic exchange coupling is obtained when the Mo thickness varies from 0.6 to 1.8 nm. The largest antiferromagnetic coupling energy of 0.036 mJ m^{-2} is found with Mo thickness of 0.8 nm. Moreover, the exchange coupling is stable after annealing at temperature up to 400 °C, making Mo more suitable than Ta for practical STT-MRAM applications. Besides, the MgO/CoFeB/Mo/CoFeB/MgO structure was adopted as the free layer by Huai et al.[100] After back-end-of-line process of 400 °C, the free layer remains perpendicularly magnetized. The thermal stability factor for a 55 nm device is established to be 52, verifying again the strong stability against annealing temperature for Mo-based structures.

In order to achieve thermally robust PMA, MgO/CoFeB/W/CoFeB/MgO structure has been widely investigated over the past few years. In 2015, Kim et al. obtained strong ferromagnetic exchange coupling in this structure when the thickness of W spacer layer ranges from 0.25 and 0.55 nm, while a transition from ferromagnetic coupling to antiferromagnetic coupling occurs at W thickness of 1.15 nm.[95] After annealing at 400 °C, the thermal stability factor of the MgO (2 nm)/CoFeB (1.5 nm)/W (0.55 nm)/CoFeB (1.2 nm)/MgO (2 nm) structure is calculated to be 78 when the device diameter is 20 nm, which is about 2.7-fold of the single-interface structure MgO (2 nm)/CoFeB (1.5 nm)/W (5 nm), as shown in Figure 6b. Moreover, after annealing at 425 °C, the W-based double-interface structure remains strong PMA, while a clear decrease of PMA is observed for the Ta-based counterpart. The thermally robust PMA of the W-based structures is mainly attributed to the suppression of diffusion at the W/CoFeB interfaces during annealing (see Figure 6c). Besides, a thermal stability of ≈60 is obtained for MgO/CoFeB/W (0.2 nm)/CoFeB/MgO structure with 3× nm node after annealing at 410 °C.[101] These findings confirm the strong thermal stability of W-based double-interface structure and point out the possibility of achieving high-density MRAMs.

3. Modulation of HM/FM Interface for High TMR

As mentioned above, the resistance of an MTJ depends on the relative magnetization alignment of two FM layers.[21,102,103] When the magnetizations of two FM layers are in PC, the MTJ exhibits a low resistance state. When the magnetizations are in APC, the MTJ exhibits a high resistance state. This resistance difference between PC and APC is called TMR effect, and the ratio of the resistance difference is called TMR ratio, which is defined as

$$\text{TMR ratio} = \frac{R_{APC}\text{-}R_{PC}}{R_{PC}} \times 100\% \quad (3)$$

In 1975, the TMR effect was reported by Julliere, who observed that the Fe/Ge/Co junction presented a TMR ratio of 14% at 4.2 K.[7] Two decades later, Miyazaki and Tezuka[104] and Moodera et al.[105] made a conclusion that in MTJs with the

AlO_x tunnel barrier layers, TMR ratio could reach up to 18% at room temperature. However, even if a large number of efforts have been put into the optimization of AlO_x-based MTJs, the TMR ratios are still relatively low, which can be attributed to the amorphous insulating layer and incoherent tunneling.

Breakthrough occurred in the theoretical research. First-principles calculations predicted that epitaxial MTJs with ferromagnetic electrodes of Fe and tunnel barrier layers of MgO would achieve high TMR ratios.[106–108] In the Fe/MgO/Fe MTJ, the tunneling depends strongly on the Bloch state with Δ_1 symmetry, which decays with the lowest rate in MgO. When Δ_1 states in Fe and MgO match, coherent tunneling happens in MTJ, leading to the enhancement of TMR ratio. Inspired by this discovery, many endeavors have been devoted to the experimental and theoretical studies of MgO-based MTJs.

3.1. Experimental Works on TMR

3.1.1. TMR in i-MTJs

Compared to AlO_x-based MTJs, MgO-based MTJs display larger TMR ratios. In 2004, Yuasa et al. investigated the Fe/MgO (2.3 nm)/Fe MTJ and reported a TMR ratio of 180% at room temperature.[15] More intriguingly, a room-temperature TMR ratio of 220% in CoFeB (3.5 nm)/MgO (2.0 nm)/CoFeB (7.5 nm) MTJ with a Ru capping layer was realized by Parkin et al.,[14] indicating that TMR ratio increased with annealing temperature up to 350 °C in this MTJ. Since then, a large number of impressive results in MgO-based MTJs appear. Djayaprawira et al. reported that TMR ratio could reach up to 230% in CoFeB/MgO/CoFeB MTJ at room temperature, higher than that in CoFe/MgO/CoFe MTJ.[109] This high TMR is attributed to the CoFeB amorphous layers which benefit the MgO crystallization, while CoFe is in polycrystal structure. After annealing, B atoms would diffuse from the CoFeB layer to the Ta layer due to its high affinity with B atoms, further facilitating the orderly crystallizations of CoFe and MgO. In 2008, a room-temperature TMR ratio of 604% in CoFeB (4 nm)/MgO (2.1 nm)/CoFeB (6 nm) MTJ with Ta/Ru capping layers was announced by Ikeda et al.,[110] where thick ferromagnetic layers might be the reason for the high TMR ratios.

Recently, three-terminal MTJs have been realized, which could be switched by SOT. The separation of writing and reading channels in SOT-MTJ offers advantages including prolonged endurance, efficient writing operation, and high-speed readout.[111] In 2012, Liu et al. reported the spin torque switching with the spin Hall effect (SHE) in β-Ta. An i-MTJ was built with Ta (6.2 nm)/CoFeB (1.6 nm)/MgO (1.6 nm)/CoFeB (3.8 nm)/Ta (5 nm)/Ru (5 nm) stack from bottom to top.[6] The device was annealed at 280 °C in vacuum for 1 h to enhance the TMR. The charge current passing through the Ta layer switched the CoFeB magnetization, and the TMR ratio for read-out was 50%.

β-W is another promising heavy metal for SOT switching. In accordance with Pai et al., the spin Hall angle of β-W is as large as –0.3, efficient to reverse the orientation of in-plane magnetized CoFeB free layers in MTJs.[112] To demonstrate the efficiency of the SHE in β-W for spintronic applications, a three-terminal device with IMA was fabricated, composed of a W microstrip and a CoFeB/MgO/CoFeB nanopillar MTJ on the top. Although the MTJ could be switched by SOT, the TMR ratio is only 51%, not desirable enough for spintronic application.

With desirable intrinsic SHE strength,[113] Pt is expected to be a kind of promising material for the bottom layer. Nguyen et al. fabricated SOT-MTJs based on the Pt (4 nm)/Hf (0.5 nm)/CoFeB (1.6 nm)/MgO (1.6 nm) stack.[114] The insertion of thin Hf layer would decrease the magnetic damping and remain the spin torque efficiency. Consequently, the SHE switching efficiency could be enhanced. After annealing at 300 °C for 30 min, the SOT-MTJ showed a TMR ratio of 80%. A following investigation of MTJs with the Pt (5 nm)/Hf (0.7 nm)/CoFeB (1.6 nm)/MgO stack was conducted by Aradhya et al.[115] After annealing at 360 °C for 45 min with the optimization of aspect ratios, the SOT-MTJ exhibited a TMR ratio of 110%. This comparison illustrates that annealing process and MTJ scale play critical roles in the TMR optimization. Moreover, thin CoFeB layers may reduce TMR ratios, since the heavy metal diffusion would induce the loss of magnetic moment. Thus, the TMR is expected to be enhanced in SOT-MTJ by using heavy metal materials with better thermal stability properties to prevent diffusions.

3.1.2. TMR in p-MTJs

Despite remarkable TMR ratios achieved in i-MTJs, the performances of i-MTJs still need to be improved in terms of the thermal stability and storage density. To make the MTJ more applicable for high-density and high-reliability MRAM, PMA as well as p-MTJ were developed.[38] The p-MTJ with Ta/CoFeB/MgO/CoFeB/Ta stack exhibited a TMR ratio of 124%.[38] Since then, a series of experiments with Ta heavy metal layer have arisen.[116–118] A comprehensive investigation by Jeon et al. revealed that the TMR ratio strongly depends on the thicknesses of both CoFeB free and reference layer in Ta/CoFeB/MgO-based MTJs.[119] A thick CoFeB layer would result in the IMA, while a thin CoFeB layer would induce the diffusion of Ta atoms into MgO. Consequently, the combination of 1.1 nm free layer and 1.59 nm reference layer can generate the highest TMR ratio of 104% in the p-MTJ. Actually, the diffusion effect of Ta atoms is a serious problem. When annealing temperature increases to 400 °C, which is required for the back-end-of-line process of integrated circuit devices, Ta diffusion would induce a thick magnetic dead layer and the instability of APC, thus, the strong reduction of the TMR ratio occurs.[120] The Ta diffusion not only degrades TMR in p-MTJ, but also causes significant magnetic moment loss and PMA deterioration, especially for the perpendicularly magnetized Ta/CoFeB/MgO films with a very thin CoFeB layer.[110,121] Discussions above validate that heavy metal layer has profound effects on TMR, and it is challenging for Ta-based MTJ to be applicable to the high-density MRAM.

To solve this problem and to achieve a desirable TMR ratio, a natural idea is to replace Ta with another heavy metal. One promising candidate is Mo. Liu et al. stated that for the Mo/CoFeB/MgO films, the strong PMA remained after annealing at 425 °C.[71] Consequently, by replacing the typical

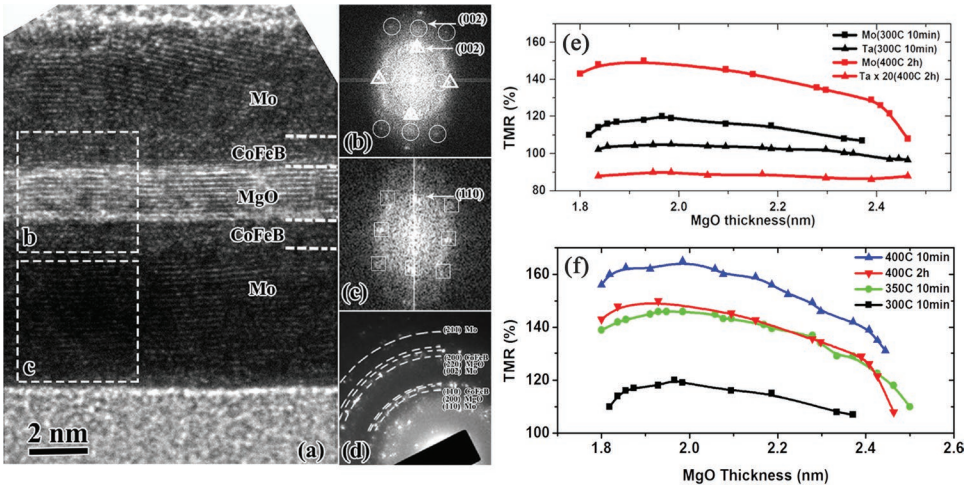

Figure 7. a–d) Structural characterization of the Mo/CoFeB/MgO/CoFeB/Mo film annealed at 400 °C. e) TMR versus MgO thickness for the Ta- and Mo-based MTJs after annealing at 300 °C for 10 min (black lines) and after annealing at 400 °C for 2 h (red lines). f) TMR for Mo/CeFeB/MgO tunnel junctions annealed at 300 °C (black line), 350 °C (green line), and 400 °C (blue line) for 10 min and 400 °C for 2 h (red line). (a–d) reproduced with permission.[71] Copyright 2014, Nature Publishing Group. (e,f) Reproduced with permission.[74] Copyright 2015, AIP Publishing Group.

Ta layer with the Mo layer, a thermally robust perpendicularly magnetized CoFeB/MgO system could be realized. This result also suggested that there was little Mo diffusion during the high temperature annealing due to the large formation energy of Mo–Fe alloys.[75] Besides, after annealing, interfaces in Mo (5 nm)/CoFeB (1.2 nm)/MgO (2 nm)/CoFeB (1.2 nm)/Mo (5 nm) stack are very neat, which is shown by the high-resolution transmission electron microscopy (HR-TEM) image in **Figure 7**a. As the CoFeB and MgO crystallizations are essential to the high TMR ratio, this result indicates that TMR in Mo/CoFeB/MgO/CoFeB/Mo MTJ is desirable.

Mo has been illustrated as a desirable heavy metal candidate for CoFeB/MgO-based MTJs.[74] It turned out that after annealing at 400 °C for 2 h, TMR ratio over 140% could be retained in a wide range of samples with Mo layers, as shown in Figure 7e. By optimizing the annealing process, TMR ratio rose to 162%, as shown in Figure 7f. On the contrary, MTJs with Ta layers exhibited the super-paramagnetic behavior and nearly vanishing magnetoresistance. This result further demonstrated the superior thermal stability and TMR in MTJs based on Mo/CoFeB/MgO structure. Besides, it has been reported that the Mo-based MTJ has a higher TMR ratio, better thermal stability, and stronger electric-field modulation in comparison with the Ta-based MTJ.[122] These results highlight the importance of the heavy metal layers adjacent to CoFeB electrodes for achieving high TMR, strong PMA, and high thermal stability in p-MTJs.

Although MTJs with Mo layers have superior characters, challenges still remain since it is hard to absorb B atoms for Mo,[75] hindering the crystallization of ferromagnetic electrodes. Moreover, thick Mo layer would crystallize and certain crystallographic orientation may impede the CoFeB crystallization,[123] while thin Mo layer is amorphous. To combine the advantages of Ta and Mo, Ta layer/thin Mo layer structure is proposed to be employed as buffer and capping layer.

Li et al. depicted the impact of Mo insertion layer on the PMA and crystallization.[124] The Ta (5 nm)/CoFeB (0.9 nm)/MgO (2 nm)/Ta (2 nm) films showed PMA at annealing temperature below 300 °C. After the insertion of a Mo layer, the Ta (5 nm)/Mo (1 nm)/CoFeB (0.9 nm)/MgO (2 nm)/Ta (2 nm) stack preserved PMA at annealing temperature up to 500 °C. The crystallization of the MgO (001) texture is improved owing to the higher annealing temperature for the Mo-inserted sample, further enhancing TMR due to the coherent tunneling preservation. Almasi et al. reported that the TMR ratio could be dramatically improved by the insertion of Mo thin layer at the Ta/CoFeB interface.[75] The Mo insert layer in the Ta/thin Mo/CoFeB/MgO/CoFeB/thin Mo/Ta stack serves as a thermal barrier to prevent the intermixing of Ta with Fe, while allowing smaller B atoms to diffuse out during the annealing process at 500 °C for 10 min. As a result, a high TMR ratio of 208% has been achieved in this p-MTJ. In addition, Mo layer can also be inserted in ferromagnetic electrodes as the spacer layer, and p-MTJ with Mo spacer layer showed a TMR ratio over 210% after annealing at 400 °C for extended hours.[100]

Apart from Mo, W has also attracted lots of attention as buffer or capping layer material. W metal has a truly high melting point (3422 °C) which boosts up the annealing stability. Consequently, W—W bonds are highly robust to prevent the W diffusion effect at the relatively high annealing temperature. During annealing, B atoms can diffuse into W layer, making W layer a B absorber. This effect benefits the crystallization of ferromagnetic layer and tunnel layer as well as the TMR ratio. A number of experimental attempts have demonstrated the superiority of W as the heavy metal material compared with Ta.

Lee et al. performed controlled experiments in two p-MTJs with W and Ta heavy metal layers.[18] Two stacks were ex situ annealed at the back-end-of-line temperature of 400 °C, as shown in **Figure 8**. Figure 8a shows the Ta-based stack, where the MgO tunneling barrier exhibited a combined structure of face-centered-cubic (fcc) crystals and amorphous structure, and the CoFeB ferromagnetic layers were revealed to be amorphous. As a result, the coherent tunneling was damaged and the TMR was reduced in this p-MTJ. On the other hand, Figure 8b shows that in the W-based stack, the

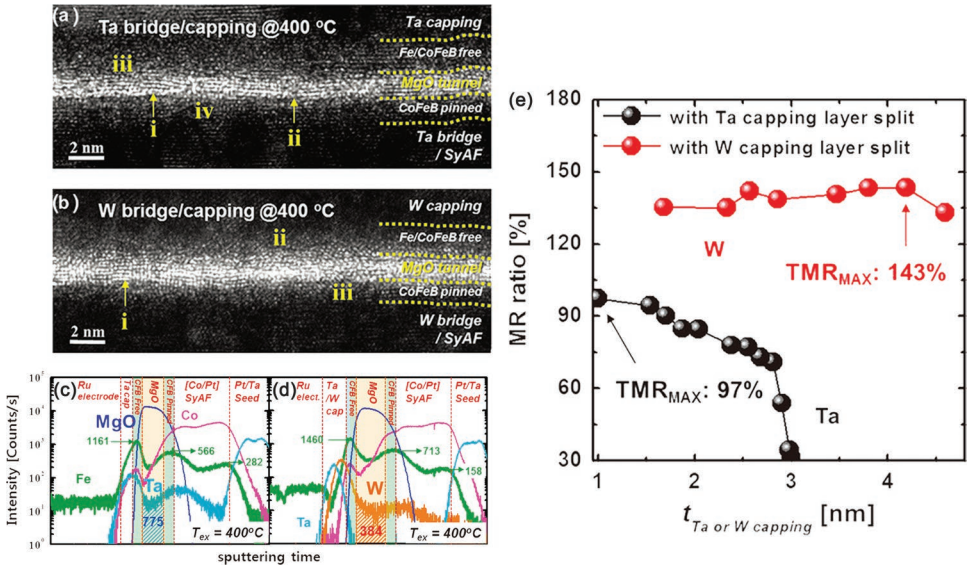

Figure 8. Dependence of fcc crystallinity of the MgO layer on the bridging and capping materials for the p-MTJs a) with Ta and b) with W. Dependence of atomic compositional depth profile of MgO tunneling barrier for the p-MTJs c) with Ta and d) with W using high-resolution secondary ion mass spectrometry (SIMS). e) Dependence of the TMR ratio on both p-MTJs with Ta and W bridging and capping layers. Reproduced with permission.[18] Copyright 2016, Nature Publishing Group.

MgO tunneling barrier has an almost complete fcc crystal structure. These HR-TEM results illustrate that the W-based p-MTJ has better MgO crystallinity than that of the Ta-based p-MTJ. The dependence of the atomic compositional depth profiles could explain the reason for MgO crystallinity difference. It is shown in Figure 8c that in the Ta-based stack, a large number of Ta atoms (775, arb. unit) diffused into the MgO layer from the nanoscale-thick Ta bridging and capping layer, while in the W-based stack, a relatively small amount of W atoms (384, arb. unit) diffused into the MgO layer, nearly half of that in the Ta-based stack. The thermal robustness of W contributed to the MgO crystallization and preserved TMR, as shown in Figure 8e. Lee et al. also reported a high TMR ratio of 163% in p-MTJ with W/Ta seed layer and W capping layer.[125] The W seed layer presented a body-centered cubic (bcc) crystallinity, and interfaces between MgO and CoFeB were very clear, indicating that both CoFeB layers were well textured with the MgO layer, thereby realizing a high TMR ratio after annealing at 400 °C. In addition, Almasi et al. unveiled a TMR ratio of 138% in p-MTJ based on W (9 nm)/CoFeB (0.95 nm)/MgO (2.4 nm)/CoFeB (1.5 nm)/W (9 nm), where W metals were used as both buffer layer and capping layer.[72] Experimental results demonstrated that after annealing at 420 °C for 10 min, the p-MTJ showed a high TMR ratio of 138% and the resistance area product (RA) of 0.5 MΩ μm^2. Subsequently, Chatterjee et al. reported that after annealing at 425 °C, the p-MTJ with W(2 nm)/Ta(1 nm) capping layer exhibited a TMR ratio of 117% and the low RA of 8 Ω μm^2, which can be attributed to the thin MgO layer.[73]

Recently, remarkable results on TMR ratio and RA have been reported,[101] as shown in **Figure 9**a. The stack structure consists of atom-thick W layers and double MgO/CoFeB interfaces. RA is as low as 7 Ω μm^2. High TMR ratio of 249% has been observed in this p-MTJ, demonstrating the occurrence of coherent tunneling in crystal MgO. This can be confirmed by the TEM image as the Figure 9c shows. After annealing at around 400 °C, clear MgO interfaces and crystallization could be observed. Atomic-resolution electron energy-loss spectroscopy (EELS) profiles show the correspondence between B and W peaks, indicating a large number of B atoms existing in the W spacer and bridging layers. Figure 9e shows that no signal of W is detected within the MgO barrier or at the CoFeB/MgO interfaces in the energy dispersive spectrometry (EDS) mapping, supporting the point that W is robust against high-temperature diffusion. In summary, the W layers not only provide a typical bcc template for the texture of adjacent CoFeB layers, but also absorb B atoms during annealing to create robust interfacial PMA. Both the crystalline structure and little atom distribution contribute to the giant TMR ratio.

Recently, SOT-MTJ with PMA (p-SOT-MTJ) has been realized in the MTJ on top of a Ta current line.[126] The p-SOT-MTJ composed of a Ta (20 nm)/CoFeB (1 nm)/MgO/CoFeB (1.5 nm)/Ta (5 nm)/Ru (7 nm) stack generates a TMR ratio of 55%, which is equivalent to that of another p-SOT-MTJ with Ta layers and SAF layers.[127] Recently, a remarkable TMR ratio of 128% has been reported in the Ta/CoFeB/MgO p-SOT-MTJ stack with a thermal stability factor of ≈47.[128] The high TMR ratio can be attributed to the careful control of the oxidation level, which induces the strong PMA.

Table 2 presents a summary of TMR ratios in p-MTJs with different heavy metals. It shows that compared to Ta-based MTJs, Mo- and W-based MTJs can present higher TMR ratios, attributed to the superior properties of Mo and W heavy metals. Both Mo and W possess high thermal stability, which prevents the diffusion of heavy metal atoms. More intriguingly, W is a good absorber of B atoms, benefiting the CoFeB crystallization.

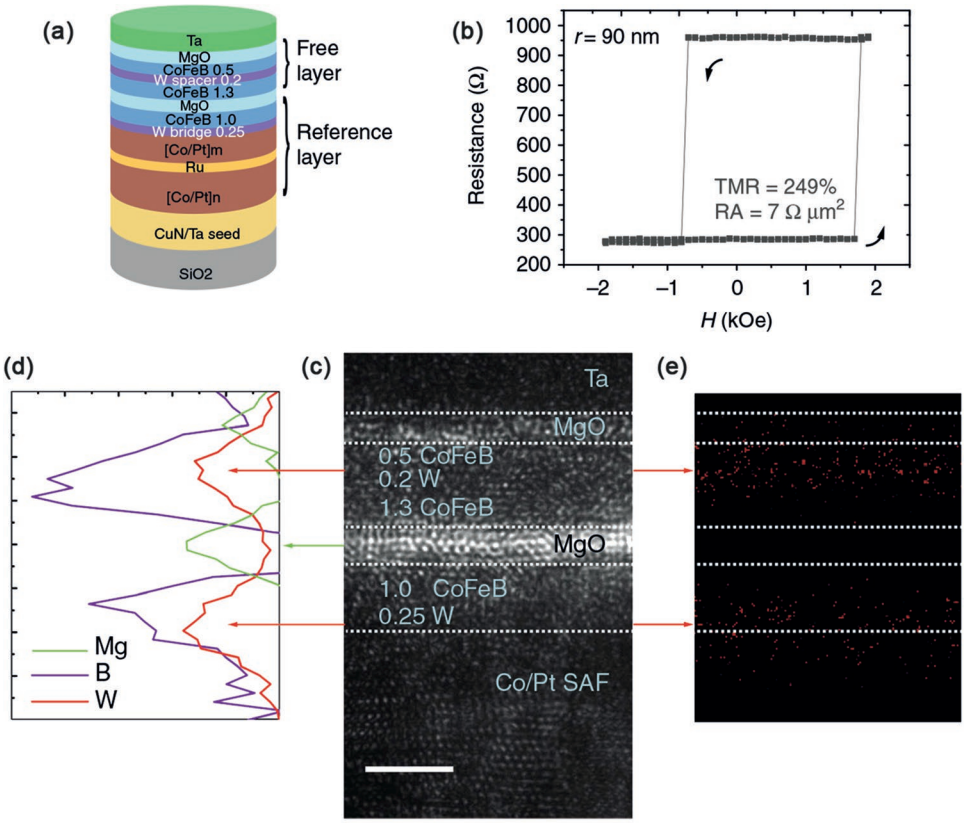

Figure 9. a) Structure of the p-MTJ stack. b) Magnetoresistance as a function of out-of-plane magnetic field. c) TEM image that profiles the crystallization. d) EELS intensities of magnesium (Mg), B, and W. Arrows show the positions of the same layer in the two figures. e) EDS mapping of the p-MTJ stack, where W is in red. Reproduced with permission.[101] Copyright 2018, Nature Publishing Group.

3.2. Theoretical Works on TMR

As a host of experiments have demonstrated the influence of heavy metal materials on TMR, theoretical studies also make progress.[129,130] Zhou et al. reported the influence of heavy metal on CoFe/MgO/CoFe MTJ by ab initio calculations.[131] Properties in MTJs capped by two kinds of heavy metals, Ta and Mo, were compared from the aspect of spin-resolved transport and TMR ratios. There are two channels in PC, majority- to majority-spin ($G_{PC}^{\uparrow\uparrow}$) channel and minority- to minority-spin ($G_{PC}^{\downarrow\downarrow}$) channel. Coherent tunneling dominates in $G_{PC}^{\uparrow\uparrow}$ channel while resonant tunneling dominates in $G_{PC}^{\downarrow\downarrow}$ channel. By comparing the transmission spectra, it is found that coherent tunneling in Mo-capped MTJ is stronger than that in Ta-capped MTJ, while resonant tunneling in Ta-capped MTJ is stronger than that in Mo-capped MTJ. **Figure 10**a shows that TMR ratio in Mo-capped MTJ is higher than that in Ta-capped MTJ at the equilibrium state, due to the strong coherent tunneling

Table 2. TMR ratios in p-MTJs with varying heavy metal materials.

Heavy metal	$t_{free\ layer}$ [nm]	$t_{reference\ layer}$ [nm]	t_{MgO} [nm]	T_a [°C]	SAF	TMR [%]	Ref.
Ta	1.7	1.0	0.85	300	No	124	[38]
Ta	1.05	1.59	1.0	–	Yes	104	[119]
Ta	1.5	0.8	1.5	300	No	128	[128]
Ta/thin Mo	1.5	0.85	0.9	500	No	208	[75]
Mo	1.6	0.8	1.95	400	No	162	[74]
Mo	1.2	1.2	1.6	350	No	120	[122]
W	1.0	1.4	1.2	400	Yes	163	[125]
W	1.5	0.95	2.4	420	No	138	[72]
W/Ta	1.4	1.2	–	425	Yes	117	[73]
W inserting	1.3 and 0.5	1.0	0.8	390	Yes	249	[101]

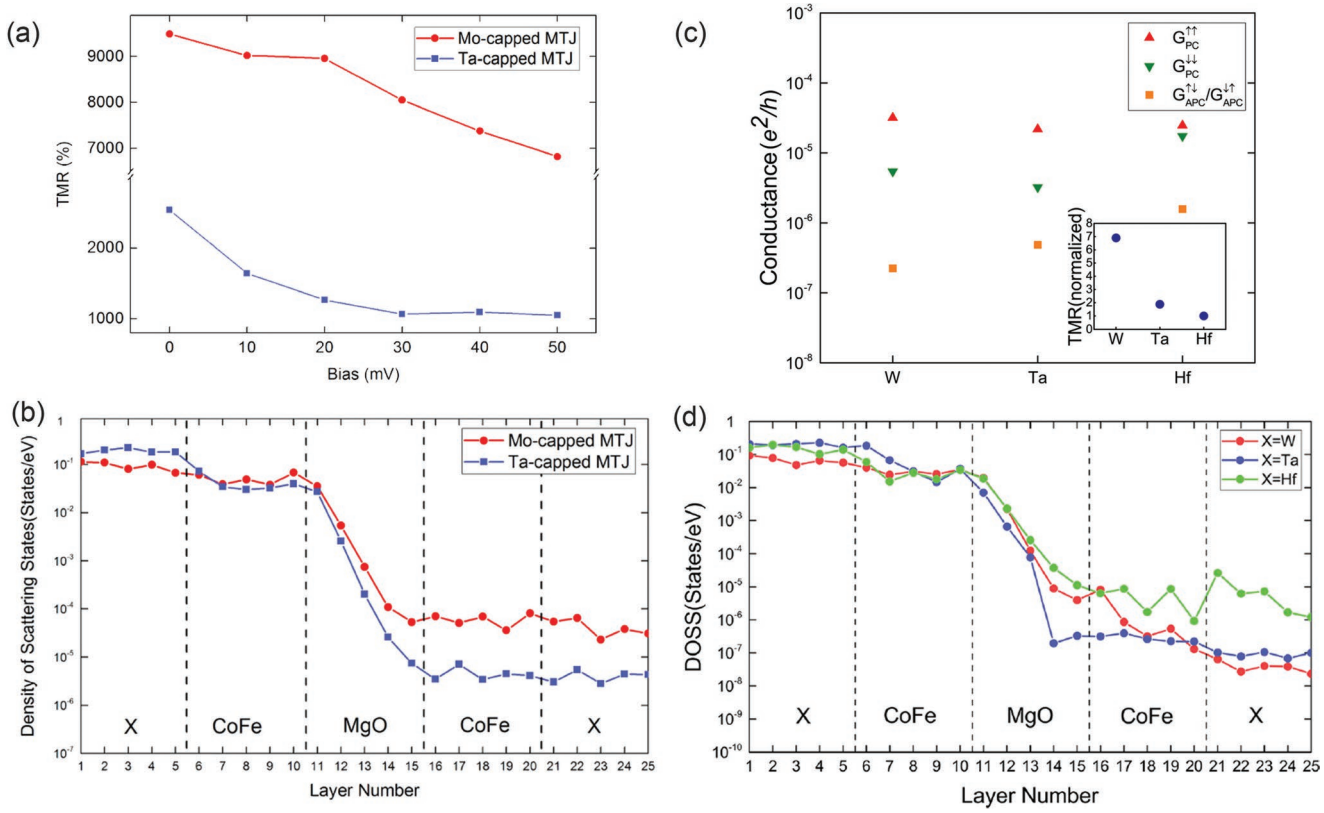

Figure 10. a) TMR ratios versus voltage bias for Mo-capped MTJ (red circles) and Ta-capped MTJ (blue squares). b) DOSS of Δ_1 symmetry in real space for Mo-capped MTJ (red circles) and Ta-capped MTJ (blue squares) in majority-to-majority-spin channel in PC. c) Spin-resolved conductance in MTJs with different heavy metal materials. The inset shows normalized TMR. d) DOSS of Δ_1 symmetry in real space for W-capped MTJ (red circles) in majority-to-minority-spin channel in APC. (a,b) Reproduced with permission.[131] Copyright 2017, IEEE Publishing Group. (c,d) Reproduced with permission.[132] Copyright 2016, AIP Publishing Group.

in $G_{PC}^{\uparrow\uparrow}$ channel of Mo-capped MTJ. This can be confirmed by layer-resolved density of scattering states (DOSS) of Δ_1 symmetry states, as Δ_1 components dominate the tunneling in MTJs with the MgO barrier layer. Results are shown in Figure 10b. DOSS in Mo-capped MTJ terminates above 10^{-5} orders of magnitude, while that in Ta-capped MTJ terminates below 10^{-5} orders of magnitude, explaining the high conductance in PC and high TMR ratio of Mo-capped MTJ. Bias influence was also considered as shown in Figure 10a, turning out that when 50 mV bias was applied, TMR ratio in Mo-capped MTJ dropped by 28%, while that in Ta-capped MTJ declined by 66%. The reason is that coherent tunneling in $G_{PC}^{\uparrow\uparrow}$ channel is relatively robust against bias, while resonant tunneling in $G_{PC}^{\downarrow\downarrow}$ channel is apparently sensitive to bias. When the bias is applied, the G_{PC} in Mo-capped MTJ remains relatively stable, however, the G_{PC} in Ta-capped MTJ decreases sharply. This study illustrates that TMR in Mo-MTJ is robust against the voltage bias.

Besides, MTJs with heavy metal of W and Hf were also studied.[132] Compared to TMR in Ta-capped MTJ, a more remarkable TMR in W-capped MTJ was predicted by calculations, as shown in Figure 10c. Different from Mo-capped MTJ, the high TMR ratio in W-capped MTJ resulted from the low conductance in APC. Layer-resolved DOSS were shown in Figure 10d for the $G_{APC}^{\uparrow\downarrow}$ channel. It can be found that an obvious difference appears at the outer CoFe/HM interface in $G_{APC}^{\uparrow\downarrow}$ channel. DOSS in Hf-capped MTJ terminates at the 10^{-6} orders of magnitude, while that in W-capped MTJ terminates below 10^{-7} orders of magnitude. This phenomenon was attributed to the orbital hybridization at CoFe/HM interfaces, thus affecting the transport properties. As a result, the G_{APC} of W-capped MTJ is the smallest, explaining the highest TMR ratios subsequently.

The oscillatory behavior of the TMR ratios due to thickness variations in Ta/CoFe/MgO MTJs has been researched.[133] A strong oscillation of the TMR amplitude would happen with respect to the thickness of the ferromagnetic layer, which was attributed to the quantization of the electronic structure of the ferromagnetic layers. The heavy metal layer adjoining to the ferromagnetic layer is found to amplify the oscillations at a given barrier thickness, leading to an enhancement of the TMR for thin ferromagnetic layers. The enhancement effect has two attributions. One is the combination of the wave function confinement in the CoFe layer, the other one is the shift in band offset due to the interface dipole caused by the electron depletion at the Ta/CoFe interface. Both factors suggest that the electronic structure of the ferromagnetic material, as well as the conductance and TMR, could be modulated by different capping materials.

4. Modulation of HM/FM Interface for Low Magnetic Damping Constant

Magnetic damping constant α is an important parameter for high-speed dynamics of magnetization, as it determines the speed of magnetization reversal[134] and the critical current density J_{c0} of STT switching because J_{c0} is proportional to α.[135] Usually HM materials are used as buffer layer and capping layer in magnetic thin films to generate structural asymmetry and to enhance interfacial effects, which can be used to modulate the magnetic damping constant for high-performance spintronic devices.

4.1. Magnetic Damping Constant in HM/FM Thin Films with IMA

The influence of heavy metal materials on magnetic damping constant can be investigated in ferromagnetic thin films with IMA using FMR. The magnetic damping constant α can be deduced from the fitting of frequency dependence of the line width ΔH with the following equation[136]

$$\Delta H = \Delta H_0 + \frac{\alpha}{\gamma}\omega \tag{4}$$

where γ is the gyromagnetic ratio, ω is resonance frequency, M_S is the saturation magnetization, and G, Gilbert damping factor, is obtained from the equation $G = \alpha\gamma M_S$.

In 2002, Mizukami et al. investigated the magnetic damping constant in HM/NiFe (Py)/HM structures with HM of Cu, Ta, Pd, and Pt through FMR method.[137] The thin film structures were grown on glass substrate by magnetron sputtering and the thicknesses of capping and buffer HM layers are 5 nm. The G values for Pd and Pt increase with decreasing Py thickness, while the G values for Ta and Cu are constant of around 0.9×10^8 s^{-1}, independent of Py thickness and smaller than those of Pd and Pt, as shown in **Figure 11**. The G values for Ta and Cu are in the same order with the bulk value around 0.7×10^8 s^{-1}.[138] With the SOC between HM and permalloy, the spin-flip scattering induces the magnetic damping precession.[139] The enhancement of G values for HM = Pd and Pt is attributed to the strong SOC of Pt and Pd atoms, which can generate a strong spin-flip scattering at the HM/Py interfaces.

Tserkovnyak et al. proposed a mechanism for the magnetic damping constant in the normal metal/ferromagnetic metal structure.[140] The precession of the magnetization transfers spins from the ferromagnetic metal into adjacent normal metal, so that the enhancement of the magnetic damping constant $\alpha' = \alpha - \alpha_0$ can be expressed as the scattering matrix at the Fermi energy of a ferromagnetic metal in contact with normal metal, illustrating the experimental results of Mizukami et al. by the following equation

$$\alpha'(d) = \kappa \times \frac{1.1}{d_{Py}} \times \frac{f_0}{f(d)} \tag{5}$$

where α_0 is the bulk magnetic damping value. f_0 and $f(d)$ are the atomic magnetization of the permalloy bulk and films, respectively. κ is an adjustable parameter, which represents the number of scattering channels in units of one channel per interface atom. d_{Py} is the Py layer thickness. The experimental results of Mizukami et al. for the magnetic damping constant α and the relative magnetization f/f_0 are shown in the insets of **Figure 12** and are in good agreement with the theoretical estimation in Equation (5), as shown by lines in Figure 12.

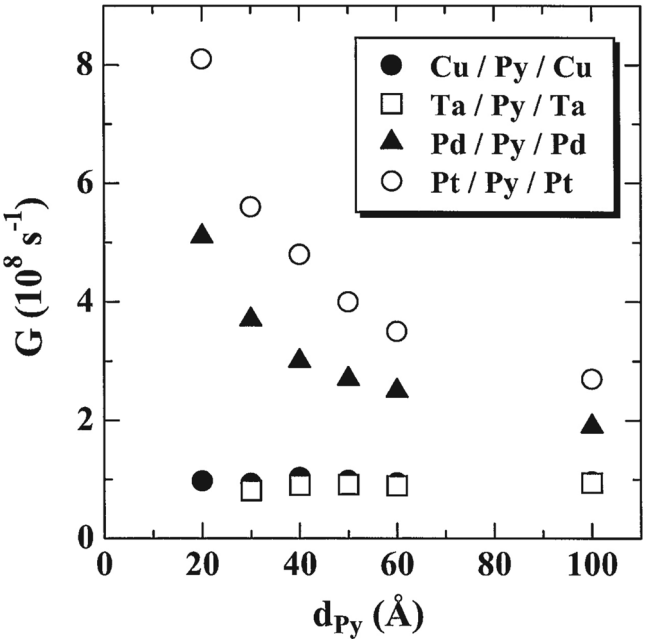

Figure 11. Gilbert damping factors as a function of Py thickness for a HM/Py/HM structure with different HMs. Reproduced with permission.[137] Copyright 2001, ELSEVIER.

4.2. Magnetic Damping Constant in HM/FM Thin Films with PMA

Recently, perpendicularly magnetized materials have attracted significant interest owing to their strong anisotropy, low switching current, and high scalability.[21,47,141] Thin film structures with PMA are currently under intensive research for several emerging spintronic effects, such as SOT,[46,142–144] domain wall motion,[145,146] and room-temperature skyrmions.[147–149] However, as the thickness of ferromagnetic layer in these structures is usually less than 1 nm, it would be too difficult to measure the dynamics using the traditional FMR method.

In order to investigate the influence of HM/FM interface on magnetic damping constant in perpendicularly magnetized FM thin film structures, a new all-optical pump-probe technique, field-dependent time-resolved magneto-optical Kerr effect (TR-MOKE) measurement,[150–152] has been proposed, providing a new method to deduce the magnetic damping constant for ferromagnetic thin film structures. The sketch map in **Figure 13**a shows a modification of the effective field H_K^{eff} as a result of the applied field H when the sample is probed prior to excitation. Then the fast demagnetization process occurs due to the pulsed laser excitation. The magnitude, the direction of the magnetization M, and the anisotropy

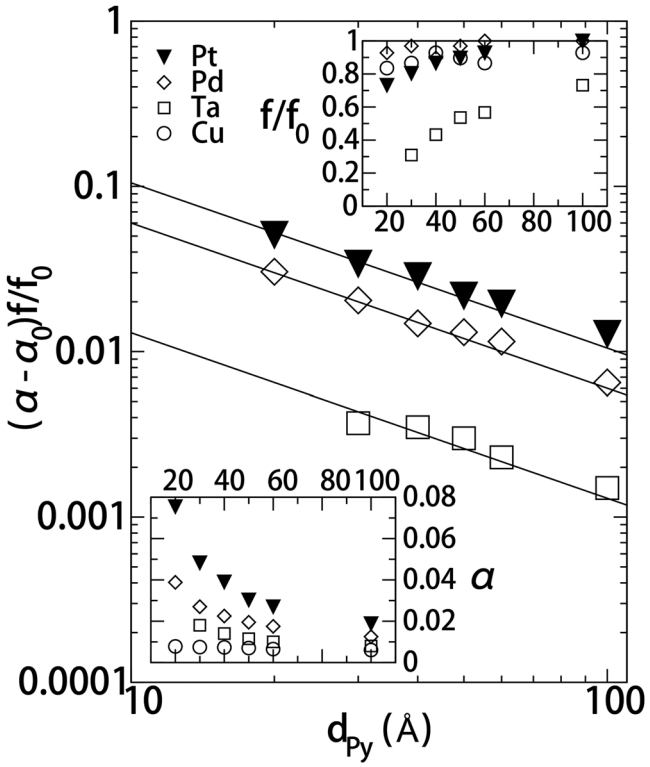

Figure 12. Theoretical results from Equation (5) with $\kappa = 1.0$, 0.6, and 0.1 are shown by the lines. The data in the two insets are derived from measurement. Insets: Measured magnetic damping constant α (lower inset) and the relative magnetization f/f_0 (upper inset) in a HM/Py/HM structure with different permalloy thickness d_{Py}. Reproduced with permission.[140] Copyright 2001, American Physical Society.

field H_K change since the lattice is modified by the laser heat, thereby altering the equilibrium orientation. M starts to precess around the reestablished equilibrium as the electronic thermal bath equilibrates with lattice (Figure 13b). After the heat diffuses away, a slower relaxation follows and H_K is restored, but the precession continues because of the initial displacement of M (Figure 13c). These relaxation processes are related to the specific heats and the coupling between different energy systems.

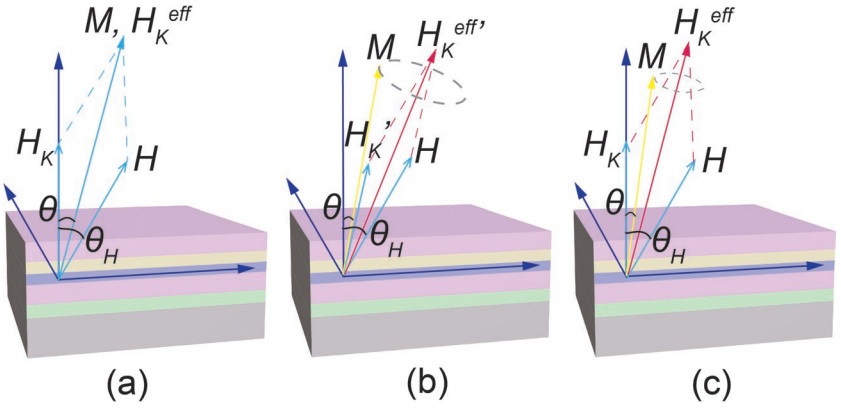

Figure 13. Damping precession process. Reproduced with permission.[159] Copyright 2017, American Institute of Physics.

The time-domain TR-MOKE signals are fitted by the following equation[153]

$$\theta_k = a + be^{-\frac{t}{t_0}} + c\sin(2\pi ft + \varphi)e^{-\frac{t}{\tau}} \quad (6)$$

where $a + be^{-\frac{t}{t_0}}$ represents an exponential decay background, c and f are the amplitude and the frequency of the magnetization precession, respectively, φ donates the initial phase of the oscillation, and τ stands for the relaxation time related to the field-dependent damping α by the relation $\alpha = 1/(2\pi f\tau)$.

Based on the field-dependent damping results, the effective damping α_{eff} can be deduced from the following equations[154,155]

$$\tau^{-1} = |\gamma|\,\alpha_{eff}\frac{H_1 + H_2}{2} \quad (7)$$

$$H_1 = H\cos(\theta_H - \theta) + H_K^{eff}\cos(2\theta) \quad (8)$$

$$H_2 = H\cos(\theta_H - \theta) + H_K^{eff}\cos^2\theta \quad (9)$$

where $|\gamma|$ is the absolute gyromagnetic ratio from the TR-MOKE fitting results, θ_H is the angle of the applied field H with respect to the film normal direction, and θ is the angle between the magnetization vector and the film normal direction.

In the previous studies, the magnetic damping constant was mostly analyzed by the thickness variation in the ferromagnetic thin film structures with a strong interfacial PMA[150,154,156] and a series of studies have focused on its correlation with interfacial PMA.[157,158] In 2017, Zhang et al. investigated the dependence of magnetic damping constant on different capping HM materials for sputtered Ta (2 nm)/Pt (3 nm)/Co (0.8 nm)/capping layer (2 nm)/Pt (3 nm) stacks, where the capping HM materials are W, Ta, and Pd.[159] Three HM materials have been explored through measurements performed by TR-MOKE. The beam wavelength and the pump beam fluence are set to 800 nm and 4 mJ cm^{-2}, respectively. The probe beam, whose intensity is much less than that of the pump beam, is almost normally incident on the film surface. TR-MOKE results are obtained with an applied field H, varying from 5 to 15 kOe. The angle θ_H between the applied field and the film normal direction is set to be 71°. **Figure 14** presents the field-dependent damping α of each sample with the applied field values varying from 5 to 15 kOe. In comparison with the Pd-capped sample, the W-capped sample has a lower damping value of around 0.03–0.04, while the Ta-capped sample shows a higher damping value of 0.06–0.08. Based on the field-dependent experimental data, α_{eff} could be obtained as 0.033, 0.063, and 0.054 for W, Ta, and Pd, respectively (**Table 3**). Although it has been reported previously in other material systems that Pd and Pt contribute more to the damping in contrast with Ta,[137,140]

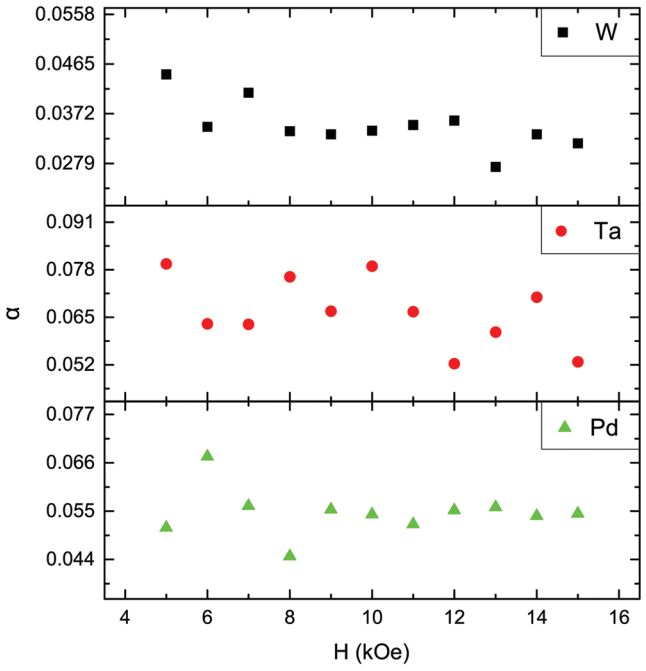

Figure 14. The field-dependent damping α as a function of the applied field for Ta (2 nm)/Pt (3 nm)/Co (0.8 nm)/capping layer (2 nm)/Pt (3 nm) stacks with capping HM materials W, Ta, Pd. Reproduced with permission.[159] Copyright 2017, American Institute of Physics.

Ta-capped stack presents a relatively large α_{eff} compared with Pd and W in Pt/Co/HM trilayered structure.

In order to explain these results, further theoretical analysis was performed for the influence of capping HM materials on magnetic damping constant and the origins of magnetic damping constant were elucidated by examining the physical contributions of different capping materials. The intrinsic damping α_{in} can be characterized as[160]

$$\frac{1}{|\gamma|M_s}\mu_B^2 D(E_F)\frac{(g-2)^2}{\tau} \tag{10}$$

As the last term $(g-2)^2/\tau$ is proportional to ξ^2/W,[161] the following equation is obtained

$$\alpha_{in} \approx \frac{1}{|\gamma|M_s}\mu_B^2 D(E_F)\frac{\xi^2}{W} \tag{11}$$

where $(g-2)^2$ is the deviation of the g factor from the free-electron value, $1/\tau$ is the ordinary electron orbital scattering frequency, μ_B is the Bohr magneton, ξ is the spin–orbit constant from the spin–orbit coupling influence of two interfaces in Pt/Co/HM stacks,[162] W is the d bandwidth from the spread of density of states (DOS) projected onto the d orbital, $D(E_F)$ is the total DOS at the Fermi energy projected onto the d orbital. Both of them are obtained from the first-principles calculations in the Pt/Co/HM stacks based on the Vienna ab initio simulation package[163,164] (see **Figure 15** and Table 3). As a main influence on the intrinsic damping, the magnon-electron scattering (MES) facilitates an energy transfer from magnetic sub-systems to nonmagnetic sub-systems, resulting in a capping-material-dependent contribution to α_{eff}. MES not only depends on the spin–orbit coupling relating to ξ, but also can be influenced by the hybridization of Co/HM interface which changes $D(E_F)$ and W.[161,165,166] The results suggest that the as-calculated theoretical estimations of the intrinsic damping follow the same trend of the as-measured effective damping (Table 3) and reach a conclusion that a lowest damping value is obtained for ferromagnetic thin films with a W capping layer.

In summary, the magnetic damping constant is sensitive to the HM/FM interface, as a result of the SOC and interfacial hybridization between FM and HM materials. The modulation of HM/FM interface makes it possible to design ferromagnetic multilayers with desirable low damping constant, which can reduce the critical current density of STT switching.

5. Modulation of HM/FM Interface for Low-Power SOT Switching

Although STT-MRAM has demonstrated great potentials as advanced nonvolatile, ultradense, and low-power memories, several challenges still remain to be solved. For instance, the intrinsic asymmetric switching can lead to a large tunneling current through the insulating barrier in the STT writing scheme, which may induce the breakdown of the barrier layer. Besides, the coupled read and write paths could cause unexpected switching by a small read current. Furthermore, the switching speed of STT is severely constrained by its long incubation time.[45]

As an alternative, SOT switching can provide solutions to the issues of STT-MRAM mentioned above. SOT originates from SOC, a relativistic interaction between the intrinsic electron spin and the magnetic field seen by the moving electron.[167] Charge currents flowing through nonmagnetic materials (NMs) with strong SOC, such as HM and topological insulator, can be converted into spin currents, which exert SOT on the adjacent FM layer to switch its magnetization. **Figure 16** shows the schematic of the typical spin–orbit torque magnetic random-access memory (SOT-MRAM), where an MTJ is fabricated on the top of an HM layer. The reversal of the free layer is realized

Table 3. Experimental and calculation results of Ta (2 nm)/Pt (3 nm)/Co (0.8 nm)/heavy metal (2 nm)/Pt (3 nm) thin film structures.

Heavy metal	α_{eff}	M_s [emu cm^{-3}]	$\lvert\gamma\rvert$ [Grad (s × Oe)$^{-1}$]	ξ [eV]	W [eV]	D (E_F) [states eV^{-1}]	$\frac{D(E_F)\xi^2}{\lvert\gamma\rvert M_s W}$
W	0.033	2090	0.0191	0.95	18.5	32.6	0.04
Ta	0.063	2034	0.0180	0.90	11	28.9	0.065
Pd	0.054	1926	0.0185	0.79	12	34.1	0.052

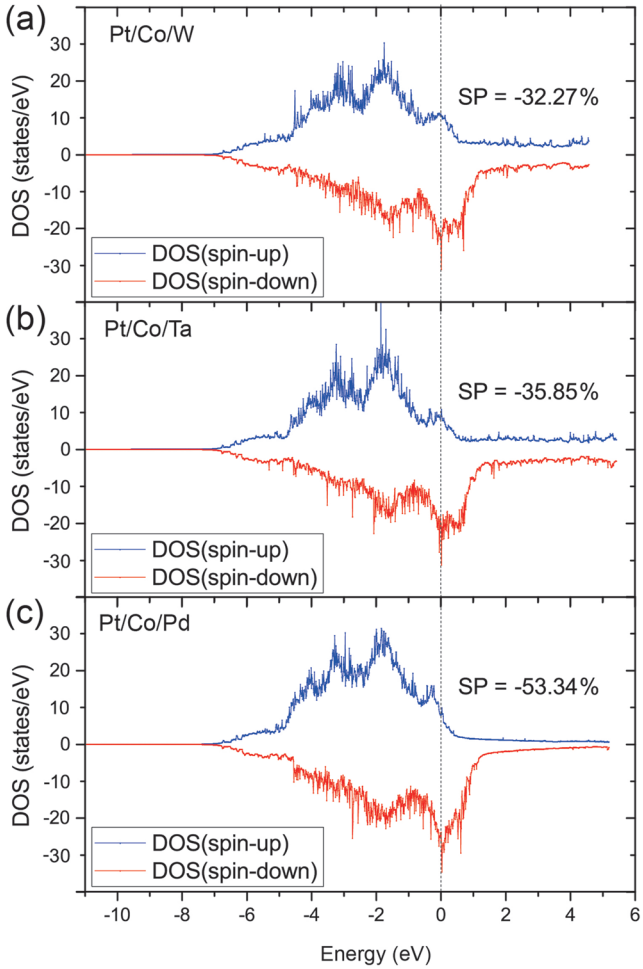

Figure 15. Majority-spin (positive) and minority-spin (negative) DOS on the d orbital in a) Pt/Co/W, b) Pt/Co/Ta, and c) Pt/Co/Pd thin film structures, where SP is the spin polarization at the Fermi energy (which is set to zero). Reproduced with permission.[159] Copyright 2017, American Institute of Physics.

by applying an in-plane current in the HM while the reading is achieved by sending a small current through the MTJ.[6,168] On the one hand, due to the decoupled write and read paths together with the greatly reduced current through the insulating barrier, the read reliability and stability of an MTJ are largely improved. On the other hand, the incubation time of p-MTJs can be eliminated by SOT, indicating the high speed of this scheme.[169–171] Note that though both in-plane and perpendicular MTJs can be switched by SOT, p-MTJs are favored because of their better scalability.[172,173] Moreover, SOT has been shown to effectively drive chiral domain walls and magnetic skyrmions,[174–176] exhibiting the broad prospect in high-density racetrack memories (RMs).[10,12] Therefore, extensive investigations have been performed to SOT over the past decade.

5.1. Origin of SOT

With the short history of a decade, the origin and the microscopic mechanism of SOT are still under investigation. But it is basically accepted that there are two main effects, the bulk SHE and interfacial Rashba effect, contributing to the generation of SOT.

SHE was first theoretically predicted in 1971,[177] but it was not observed until 2004 due to the lack of electrical signal.[178] As SHE can function as a spin current source, which is one of the focuses of spintronics, this effect has been broadly exploited ever since. The physical picture of bulk SHE is illustrated in Figure 16a. When an in-plane charge current $\boldsymbol{J}_c$ is injected into the HM, a spin current $\boldsymbol{J}_s$ with polarization σ is generated and accumulates at the HM/FM interface, thus exerting SOT on the adjacent FM layer. Note that these three vectors are mutually orthogonal and satisfy $\boldsymbol{J}_s = \frac{\hbar}{2e}\theta_{SH}(\boldsymbol{J}_c \times \boldsymbol{\sigma})$,[112] where θ_{SH} is the spin Hall angle describing the charge to spin conversion efficiency. Since the direction of $\boldsymbol{J}_s$ is along z direction in this HM/FM bilayer structure, an in-plane charge current will result in the spin accumulation with an in-plane polarization due to SHE. To date, SHE in bulk materials is attributed to three main mechanisms including the intrinsic deflection, side jump scattering, and skew scattering, indicating various means to modulate the strength of SHE.[179]

By contrast, Rashba effect arises from interfacial SOC in the structure lack of inversion symmetry, such as HM/FM bilayer,[180,181] in which a built-in electric field $\boldsymbol{E}$ is formed. Moving electrons near the interface will experience a magnetic field $\boldsymbol{H} \propto (\boldsymbol{E} \times \boldsymbol{p})$ shown in Figure 16b, where $\boldsymbol{p}$ is the momentum of electrons, which gives rise to a spin current with polarization $\boldsymbol{\sigma}$ along the field $\boldsymbol{H}$. If no lateral symmetry is introduced, $\boldsymbol{E}$ is along z direction, thus the direction of $\boldsymbol{\sigma}$ is similar to the case of SHE.

In the early experiments, Miron et al. attributed the SOT switching to Rashba effect,[182] while Liu et al. considered SHE as the origin.[6,183] However, it is difficult to distinguish which effect is the cause of SOT, especially in the HM/FM bilayer system, where both effects may simultaneously exist.[184]

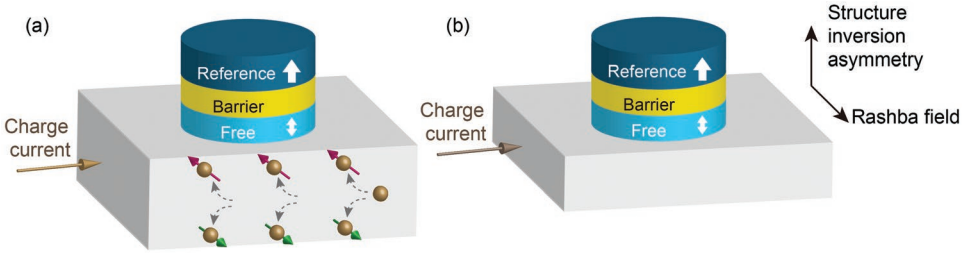

Figure 16. Schematic of typical three-terminal SOT-MRAM. The SOT originates from a) the spin Hall effect and b) the Rashba effect.

5.2. Magnetization Switching Induced by SOT

Though the origin of SOT still remains to be uncovered, SOT is generally considered consisting of two terms, the damping like torque (DLT) $\tau^{DL} \approx (\boldsymbol{m} \times \boldsymbol{\sigma} \times \boldsymbol{m})$ and the field like torque (FLT) $\tau^{FL} \approx (\boldsymbol{m} \times \sigma)$, where $\boldsymbol{m} = \frac{\boldsymbol{M}}{|M_s|}$ is the reduced magnetization with the saturation magnetization M_s, and σ is the electron polarization direction of spin polarized current arising from SOC. The impact of SOT on magnetization can be well depicted by adding the two terms in the Landau–Lifshitz–Gilbert (LLG) equation[185]

$$\frac{\partial \boldsymbol{m}}{\partial t} = -\gamma\, \mu_0 (\boldsymbol{m} \times \boldsymbol{H}_{\text{eff}}) + \alpha \left(\boldsymbol{m} \times \frac{\partial \boldsymbol{m}}{\partial t} \right) + \gamma\, \mu_0\, H_{\text{SOT}}^{\text{DL}} (\boldsymbol{m} \times \boldsymbol{\sigma} \times \boldsymbol{m}) + \gamma\, \mu_0\, H_{\text{SOT}}^{\text{FL}} (\boldsymbol{m} \times \boldsymbol{\sigma}) \tag{12}$$

where $\boldsymbol{H}_{\text{eff}}$ denotes the effective field, including all magnetic field contributions, such as the anisotropy field, demagnetization field, exchange field, and Zeeman field. γ is the gyromagnetic ratio, μ_0 is the vacuum permeability, and α is the Gilbert damping factor. $H_{\text{SOT}}^{\text{DL}} = \frac{J_{\text{SOT}} \theta_{\text{SH}} \hbar}{2 e t_{\text{F}} \mu_0 M_s}$ and $H_{\text{SOT}}^{\text{FL}} = \eta H_{\text{SOT}}^{\text{DL}}$ represent, respectively, the current-dependent proportionality constants for DLT and FLT of SOT with reduced plank constant $\hbar$ and electron charge e. t_{F} is the thickness of the adjacent FM layer, J_{SOT} is the SOT current density, and η is the ratio between the strength of these two torques.

Since the spin polarization direction $\boldsymbol{\sigma}$ is transverse to the initial magnetization $\boldsymbol{m_0}$, SOT can be maximum at the beginning, which means that the incubation time could be eliminated,[170,186] thus high speed and low power switching are promising. However, only 90° switching can be realized with sole SOT, which can be clarified by the macromodel approximation, as the static solution of Equation (12) is $\boldsymbol{m} = \boldsymbol{\sigma}$ if a large enough J_{SOT} is applied. After SOT current is turned off, the magnetization $\boldsymbol{m}$ will randomly precess to $+z$ or $-z$ direction because of thermal agitation. Therefore, switching induced by SOT alone is not deterministic. To address this issue, generally, an in-plane magnetic field is required to break the symmetry of SOT.[6,170] When the field is incorporated, the solution to Equation (12) is different as $\boldsymbol{m}$ will finally align in nearly the xy-plane with m_z being slightly negative (assume initial magnetization points along $+z$) as SOT current is on, thus deterministic switching can be realized due to the damping torque after this current is removed. Note that switching from $+z$ direction to nearly in-plane direction can be finished within 1 ns, corresponding to the fast switching feature of SOT. Over the years, switching induced by SOT within nanoseconds or even sub-nanoseconds has already been demonstrated.[170,171] Unfortunately, the necessity of an external field severely hinders the application of SOT, so several schemes have been proposed to address this issue, which will be discussed in detail in Sections 5.3 and 5.4. By contrast, initial STT is close to zero since the spin current polarization $\boldsymbol{m_p}$ is almost collinear with $\boldsymbol{m_0}$, thus plenty of precessions along the easy axis are inevitable, resulting in the long incubation time. The typical switching behavior of a perpendicular magnetic layer induced by SOT or STT is illustrated in **Figure 17**a,b, respectively, which exhibit distinct differences.

Apart from the requirement of an external magnetic field, reducing the threshold SOT current density is another challenge before translating SOT into a competing technology. In 2013, Lee et al. derived an analytical expression of this threshold current density J_{th} from a quasi-static approximation with only the DLT of SOT considered as follows[186]

$$J_{\text{th}} = \frac{2 e M_s t_{\text{F}}}{\hbar \theta_{\text{SH}}} \left(\frac{H_{\text{K,eff}}}{2} - \frac{H_x}{\sqrt{2}} \right) \tag{13}$$

where $H_{\text{K,eff}}$ and H_x denote the effective anisotropy field and in-plane field, respectively. This formula is rather accurate with negligible FLT of SOT but fails to interpret experiments where distinct FLT is observed, e.g., in Ta/CoFeB/MgO system.[171] Interestingly, the damping constant is not contained in this expression, indicating the indirect competing relation between the DLT and damping torque $\alpha \left(\boldsymbol{m} \times \frac{\partial \boldsymbol{m}}{\partial t} \right)$, unlike the STT case. Actually, as their simulations suggest, a relatively high damping is required to achieve deterministic switching after SOT current is turned off. The expression also shows that the required SOT current could be a magnitude higher than that of STT, which will be unrealistically high for devices with large $H_{\text{K,eff}}$. The threshold current density can be greatly reduced by including a large FLT of SOT, as shown in several literatures,[169,187,188] but to realize switching within one nanosecond, SOT current density as high as ≈100 MA cm^{-2} is still required.[171]

5.3. Material Choices for HM

As previously mentioned, achieving field-free magnetization switching by low SOT current density is what researchers are struggling for in this field. Plenty of materials have been explored to realize this goal.

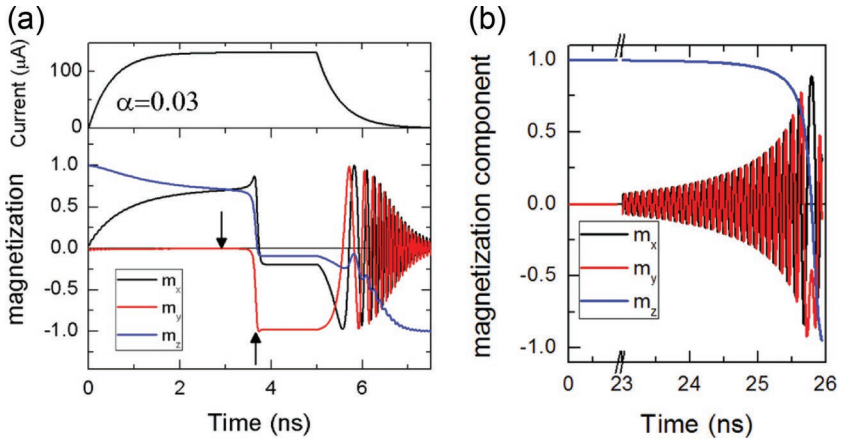

Figure 17. Typical switching behavior of a perpendicular magnetic layer induced by a) SOT and b) STT. Note that only the DLT of SOT is included in (a). Reproduced with permission.[186] Copyright 2013, American Institute of Physics.

5.3.1. Materials with Large Spin Hall Angle

A straightforward method to reduce the threshold SOT current density is to enhance the spin Hall angle θ_{SH}. To date, the most widely studied materials are pure transition heavy metals, such as Pt, Ta, and W. The measured spin Hall angles for them are about 0.07 for Pt, −0.12 for β-Ta, −0.3 for β-W.[6,183,112] These values are quite higher than that measured from nonlocal spin valve experiments and large enough to successfully manipulate the magnetization of adjacent FM layer,[189] especially in Hall bar experiments measured with long current pulses. In these experiments the switching behavior is dominated by DW nucleation and propagation and the increasing temperature in samples contributes as well.[183,190] Consequently, the required SOT current density (≈10 MA cm^{-2}) is lower than the estimated value from macrospin simulations. However, the switching behavior will eventually be single domain with the continual scaling down of p-MTJs and thermal effects will not be distinct in short pulse operations. Hence, pure heavy metals may not satisfy the demand for small MTJs with high $H_{K,eff}$ due to the high current density. For instance, to ensure the industry standard retention time of 10 years necessitates a thermal stability factor of 60, which means that for MTJs with a radius of 20 nm, the $H_{K,eff}$ should exceed 0.3 T. Under this circumstance, the estimated SOT current density will be ≈100 MA cm^{-2} or even higher.

The θ_{SH} of pure heavy metals should be further enhanced, but maybe at the expense of increasing their resistivity. Recently, Sagasta et al. unveiled that the intrinsic mechanism dominates the contribution to SHE in β-Ta, illustrating that the θ_{SH} can be linearly enhanced by increasing the resistivity.[191] Actually, the largest reported θ_{SH} for Ta (up to −0.35 ± 0.03) has been acquired in their work with the resistivity as large as 648 μΩ cm. However, from the power consumption perspective, alternative methods ought to be explored.

Metal alloys have also been widely exploited, in particular, Au alloys have shown great potentials to get larger θ_{SH}. In 2010, Gu et al. reported a large SHE in Pt-doped Au films, where the obtained θ_{SH} is 0.12 ±0.04, comparable to that of β-Ta, while the resistivity is 6.9 μΩ cm, at least 20 times smaller.[192] Theoretical calculations show that the skew scattering due to a Pt impurity in the Au (111) surface is the main cause, providing a novel way to obtain large SHE. The SHE in Au can also be enhanced with Ta impurity. In 2017, Laczkowski et al. demonstrated a θ_{SH} as high as 0.5 in $Au_{90}Ta_{10}$ alloy, and they attributed the large θ_{SH} to the side-jump scattering on Ta impurity.[193] Note that the resistivity of AuTa, 85 μΩ cm, is also much smaller than that of β phase pure transition metals. Most recently, $\theta_{SH} \geq 0.58$ has been got in the alloy $Au_{0.25}Pt_{0.75}$ with a moderate resistivity of 83 μΩ cm.[194] Differently, the large θ_{SH} in this alloy originates from the intrinsic contribution of SHE. Although θ_{SH} has been enhanced, it is necessary to verify whether high TMR ratio and PMA can be maintained simultaneously based on these materials.

From the aspect of obtaining giant θ_{SH}, topological insulators (TIs) can be one of the most promising candidates. TI is a kind of new class quantum material which behaves like an insulator in the bulk but contains conducting states on the symmetry-protected surface. Owing to the strong SOC, the spin and momentum of the moving electrons on the surface are locked to be perpendicular, resulting in a spin splitting, i.e., charge to spin conversion.[195] Note that the measured θ_{SH} of TIs is quite large. In 2014, magnetization switching induced by extremely low SOT current density (8.9×10^4 A cm^{-2}) was demonstrated in $(Bi_{0.5}Sb_{0.5})_2Te_3/(Cr_{0.08}Bi_{0.54}Sb_{0.38})_2Te$ bilayer system by Fan et al.[196] Through second harmonic measurements, the θ_{SH} of $(Bi_{0.5}Sb_{0.5})_2Te_3$ is found to be 180–450, which is nearly three magnitudes higher than that of pure transition metals. This outstanding characteristic gives a boost to the research on TIs.[197,198] However, the relatively high resistivity of TIs (≈4000 μΩ cm) is still a bottleneck of the real applications. For one thing, the power consumption is partly limited by the high resistivity; for another thing, the shunting effect may affect spin current generation in TIs. This issue can be addressed by a conductive TI, BiSb, which possesses a large θ_{SH} of 52 while the resistivity is reduced to 400 μΩ cm.[199] Moreover, DC et al. have recently demonstrated that the TI $Bi_xSe_{(1-x)}$ can be deposited using the sputtering while the spin Hall angle is maintained or even larger than that of Bi_2Se_3 grown from molecular beam epitaxy, indicating the industrial prospect of TIs.[200] It should be mentioned that thermal effects, such as ordinary Nernst effect and anomalous Nernst effect, could contribute to spurious signals during the SOT measurements. As a result, it is suggested to treat the dependence of the Hall signal on the external magnetic field carefully.[201,202]

Apart from experimental progress, theoretical studies also trigger the development of SOT. Ab initio calculation emerges as an effective method to compute the intrinsic spin Hall conductivity of various materials.[113] But generally, the calculations are convergence challenging and time consuming. In 2018, Qiao et al. presented a novel scheme by using maximally localized Wannier function interpolation,[203] which greatly improved the calculation efficiency and achieved nearly the same accuracy as previous studies.

5.3.2. Materials with Distinct Field Like Torque

Over the decade, a large body of literature has reported the DLT of SOT, with which the dynamics of magnetization is simple and direct. The origin of FLT is still a pending question, but its existence has been widely verified in experiments, especially in Ta/FM bilayer.[171,188,204,205]

Theoretical studies have been performed to evaluate the effect of FLT on magnetization switching behavior in these systems. In 2014, through macromodel simulations, Park et al. showed that with a substantial FLT whose sign stays the same with the DLT in our convention, i.e., $\eta > 0$ in Equation (12), the switching probability can be improved and the required SOT current density can be reduced.[169] Afterward, in 2015, Legrand et al. proposed that deterministic field-free switching can be achieved if the ratio between FLT to DLT satisfies $-4.35 < \eta < -1.82$.[206] The pulse rising time is critical but a precise control of pulse width is not necessary, illustrating the potential of this switching scheme in sub-nanosecond regime. However, the $\eta < 0$ case, in our convention, has not been met in almost all the previous experiments.[204] Therefore, experimental

evidences and theoretical researches are still required to verify the feasibility of this scheme.

The effect of FLT on reducing SOT current density has been recently confirmed by Fan et al. in (Pt, Ta)/CoFeB/MgO, where asymmetric SOT switching was observed once the applied in-plane field was not collinear with the SOT current direction.[207] Besides, according to Yang and co-workers, a strong FLT of SOT can give rise to oscillatory magnetization switching behavior.[204,205] Usually, magnetization is more likely to be reversed by a current with higher current density and longer pulse width. However, with the existence of a large FLT ($\eta \approx 4$ in their experiments), SOT currents with higher density or longer pulse width may result in lower switching probability, which is explained by the DW reflection or DW chirality change due to the large FLT. Through this interesting phenomenon, a deterministic unipolar SOT switching is realized by the control of the current pulse duration, providing a novel operation strategy in this field.

Up to now, several factors, such as oxidation,[208] layer thickness,[55] and annealing,[209] have been exhibited to successfully modulate the ratio η. These factors may be the reason why the η parameters reported by different groups vary a lot, even in the same material system. To practically utilize the FLT in the SOT switching scheme, a precise control of η should be ensured.

5.3.3. Antiferromagnetic Materials

Antiferromagnetic materials hold promise for storage layer in MTJs due to their intrinsic high precession frequency and zero net magnetization. These advantages make it possible to achieve ultrafast switching speed, and benefit the stability of the magnetic states. Over the years, antiferromagnets (AFM) switching induced by SOT has been demonstrated.[210,211]

On the other side, it has been realized that AFM can serve as the SOT source while simultaneously providing an exchange bias. Hence, in this system, the external magnetic field can be eliminated, which is of particular interest to practical applications. In 2016, Fukami et al. experimentally demonstrated the scheme in Co/Ni multilayers with PMA and antiferromagnetic PtMn, which exhibits a spin Hall angle comparable to Ta and provides an exchange bias.[212] Afterward, similar results have been obtained in antiferromagnetic IrMn/FM system.[213]

The spin Hall angle of AFM remains to be improved. To date, the largest reported θ_{SH} of AFM is about 0.3,[213] which requires further enhancement with the scaling down of p-MTJs. One possible solution is to utilize alternative materials with large enough θ_{SH}, whereas the AFM is just adopted to generate the exchange bias, as demonstrated by Brink et al. in Pt/Co/IrMn.[144] However, whether an insertion AFM layer will affect the performance of MTJs remains to be validated. Combining AFM and voltage-controlled magnetic anisotropy effect is another method to aid the high current density issue of SOT switching. Simulations using experimental parameters predict that the SOT current density can be decreased to 4.5 MA cm^{-2} and the power consumption can be as low as 8.5 fJ per bit.[214]

Recently, non-collinear antiferromagnetic materials, such as Mn_3Sn and Mn_3Pt, have attracted broad attention. In 2015, anomalous Hall effect (AHE) comparable to FM was first observed in Mn_3Sn by Nakatsuji et al.,[215] providing an effective way to detect the state of AFM. This is attributed to the triangular magnetic configuration of Mn_3Sn, which breaks the symmetry of a kagome lattice.[215,216] Afterward, AHE has also been demonstrated in Mn_3Pt and Mn_5Si_3.[217,218] Particularly, Liu et al. found that AHE in Mn_3Pt can be effectively tuned by a small strain due to the fragile magnetic order in this material.[217] Apart from AHE, in 2019, the contribution of non-collinear magnetic order in Mn_3Sn to SHE was demonstrated by Kimata et al.[219] This newly discovered magnetic SHE can be manipulated by an external magnetic field,[219] and the θ_{SH} of Mn_3Sn was evaluated to be $\approx 5.3 \pm 2.4\%$ by the inverse spin Hall measurement.[220] These intriguing discoveries have deepened the comprehension of antiferromagnet spintronics and provided possibility for related applications.

5.4. Methods to Achieve Field-Free SOT Switching

To achieve deterministic SOT switching, the key point is to break the symmetry of SOT. It is common to apply an in-plane external magnetic field collinear with the current direction. However, this magnetic field is an obstacle to the application of SOT. Therefore, several alternative schemes have been proposed to eliminate it.

5.4.1. Generating an Equivalent In-Plane Magnetic Field

One straightforward solution is to generate an equivalent in-plane magnetic field through novel materials or structures. In addition to the exchange bias provided by aforementioned AFM, the dipolar field from an additional in-plane magnetic layer in the stack can be used as well, which was demonstrated by Zhao et al. in 2016.[221] Note that the dominating role of dipolar field is excluded in ref. [222], where similar structures are fabricated, thus a precise design is needed.

Apart from this method, in 2017, Cai et al. reported an electric field controlled SOT field-free switching in a PMN-PT/Pt/Co/Ni/Co/Pt system structure, where PMN-PT is a ferroelectric substrate.[223] By applying a voltage on PMN-PT, a gradient of a perpendicular electric field $\boldsymbol{E_p}$ along the current direction is formed, thus the moving electrons at different positions experience different SOC. As a consequence, a spin density gradient, which acts as an in-plane magnetic field, is generated and exerts an extra torque to deterministically switch the magnetization.

The interlayer exchange coupling between an in-plane FM layer and a perpendicular FM layer can also provide an in-plane magnetic field $\boldsymbol{H}_{IEC}$, collinear with the orientation of the magnetization of the in-plane FM layer. Thanks to $\boldsymbol{H}_{IEC}$, SOT field-free switching has been realized in several works.[224,225] Note that the spacer layer between these two FM layers should exceed certain thickness, below which the IEC is too strong. It is still under dispute on how to implement this method in p-MTJs system.

5.4.2. Generating a Perpendicular Magnetic Field

Apart from the in-plane field, SOT deterministic switching can also be implemented with the aid of a perpendicular magnetic

field. In 2014, Yu et al. demonstrated SOT field-free switching in Ta/$Co_{20}Fe_{60}B_{20}$/TaO_x structure.[226] The TaO_x layer is wedge-shaped, thus a lateral structural asymmetry is introduced in this system. When an in-plane current is injected into the bottom Ta, an additional SOT effective field $\boldsymbol{H_z}$ emerges due to the Rashba effect, which breaks the symmetry of SOT and results in the deterministic switching. But it may be difficult to apply this scheme in practical chip fabrication due to the requirement for a wedge-shaped device.

In 2018, Ma et al. presented the switching of a perpendicularly magnetized ferromagnetic layer in the absence of magnetic fields by competing spin currents in Pt/W/CoFeB/MgO stack.[227] As is well-known, the signs of spin Hall angle in Pt and W are opposite, thus the spin currents generated in these two layers will cancel out at certain degree, depending on the thicknesses of the Pt and W layers. However, SOT field-free switching is observed in their samples when a large current is applied, even in the Pt (3 nm)/W(1 nm)/CoFeB(1 nm)/MgO sample, where the measured θ_{SH} and SOT effective fields are negligibly small, which cannot be explained by conventional SOT mechanism. To capture the novel phenomenon, a perpendicular magnetic field $H_z \propto J$ observed in their experiments, is included in LLG equation together with the conventional SOT, hence, the SOT field-free switching can be well reproduced. Therefore, the competing spin currents may induce a new mechanism, which manifests as a perpendicular magnetic field but still remains unclear.

5.4.3. Engineering a Tilted Anisotropy

In addition to introducing a lateral asymmetry, wedge-shaped geometry can be used to engineer a tilted anisotropy to achieve SOT field-free switching.[228] In 2015, You et al. fabricated Ta/CoFeB/MgO samples, where MgO was completely etched while the CoFeB layer was wedge-shaped. The spins aligning in the wedge result in a tilted anisotropy, thus the hard plane deviates from the *xy*-plane. Since SOT current tends to align magnetization to nearly $\pm\boldsymbol{\sigma}$, which has crossed the hard plane on this occasion, magnetization will precess into the other equilibrium state owing to the damping torque after turning off the current. Mass production is also an obstruct this scheme faces.

5.4.4. Generating Spin Currents with Perpendicular Component at Interfaces

The symmetry of SOT can also be broken by generating spin currents with perpendicular component. In 2018, Baek et al. proposed a new mechanism to generate spin currents at the interface between an in-plane FM layer and an NM spacer layer.[222] The structure of their samples is FM/Ti/CoFeB/MgO, where the bottom FM layer with IMA and the top CoFeB layer with PMA are separated by an NM spacer layer Ti which shows insignificant spin current generation. When a current is injected into the bottom FM/Ti bilayer along the *x* direction, the top CoFeB can be deterministically switched without external magnetic fields. Second harmonic measurements show that the polarization $\boldsymbol{\sigma}$ of the generated spin currents is along *y* direction, which is inconsistent with the anticipated bulk effect, i.e., $\boldsymbol{\sigma} = \boldsymbol{m}$, where $\boldsymbol{m}$ is the magnetization of the bottom FM layer (along *x* direction). Therefore, it is the interface of the bottom FM/Ti that generates the spin currents. Besides, the spin currents possess a *z* component that is antialigned with the perpendicular magnetization, leading to SOT field-free switching in their experiments. Similar results can be obtained at Co/Pt and Co/Cu interfaces, as recent transport calculations suggest.[229] Therefore, in the widely studied HM/FM bilayer system, the contributions from the interface ought to be considered more carefully.

5.4.5. Field-Free Switching through the Interplay of SOT and STT

In the conventional SOT-MRAM, the write operation is through SOT while the read operation is implemented by injecting a small STT tunneling current into the MTJs. Since STT can be used to break the symmetry of SOT, the combination of these two effects will enable SOT field-free switching while the STT current density can be largely reduced.

The schematic of this method, proposed by Wang et al. and Brink et al.,[111,230] is shown in **Figure 18**a. As can be seen, the free layer will be reversed by the interplay of SOT and STT. The significant merit of this method is that no changes are required to the structures or materials of conventional SOT-MARM, making it applicable for practical fabrication. Moreover, through this joint effect, some intrinsic issues for the two mainstream techniques, including long incubation time, large tunneling current density for STT, as well as the necessity of an external magnetic field for SOT, can be settled at the same time.

The first experimental demonstration of this scheme has been recently performed by Wang et al. in the Ta-based p-MTJ system.[188] In their experiments, the SOT and STT currents were simultaneously applied to the devices. Thanks to the effect of STT, deterministic field-free switching can always be observed, even when STT current density is as low as 1 MA cm^{-2}, as shown in Figure 18c,d. Note that the SOT current density utilized in their experiments is an order lower than that calculated from Equation (13). Macromodel simulations illustrate that the required SOT current could be largely reduced with the FLT of SOT, as shown in Figure 18b. Since the interface between HM and FM may contribute to the FLT, it is vital to further investigate the role of it. Furthermore, because of the direct connection between the Ta and the CoFeB bottom layer, the presence of strong SOT is verified when a two-terminal STT current is injected. In this case, the field-free switching of p-MTJs is induced by the interplay of SOT and STT as well. Hence, an energy and area efficient two-terminal SOT devices can be realized. Similar results have been observed in ref. [231].

5.4.6. Shaping the Magnetic Energy Landscape

Another scheme compatible with current magnetic recording technology without requiring any novel material was proposed by Kazemi et al. through micromagnetic studies.[232] In the proposed scheme, the FM layer is perpendicularly magnetized but with an elliptical cross-section whose major axis encloses a θ degree with the

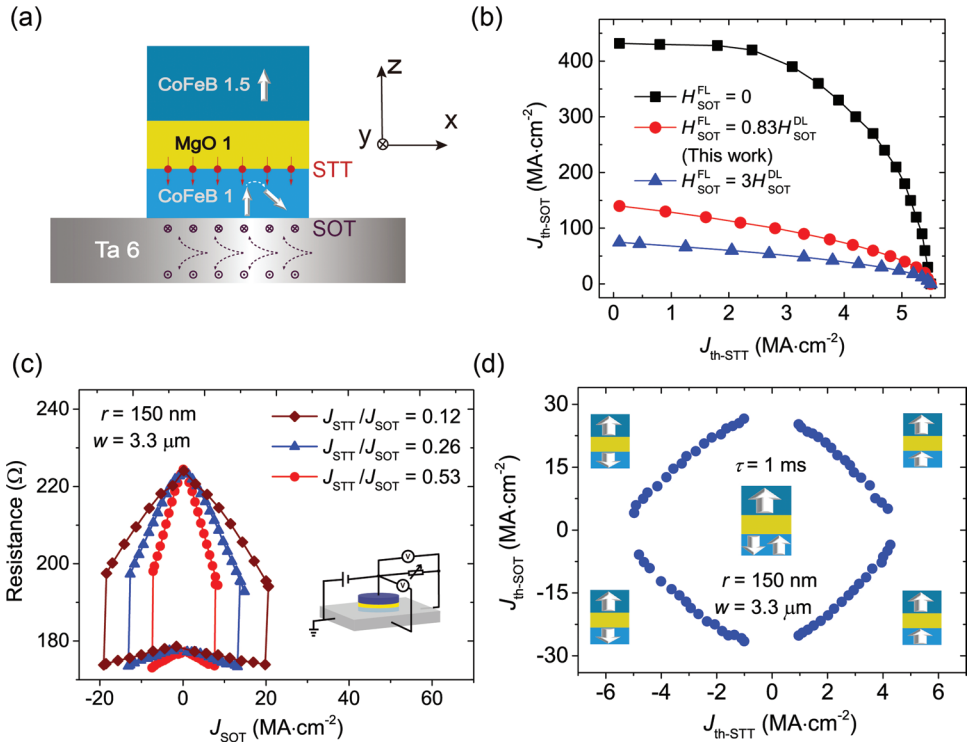

Figure 18. SOT field-free switching through the interplay of SOT and STT. a) A schematic of SOT + STT. b) The relationship between the threshold SOT and STT current density with varying FLT to DLT ratios. c) Magnetoresistance changes with varying STT to SOT current density ratios. d) Threshold SOT current density measured as a function of threshold STT current density. Reproduced with permission.[188] Copyright 2018, Nature Publishing Group.

SOT current direction. Therefore, the magnetic energy landscape becomes asymmetric with the current flow and SOT. By precisely controlling the SOT current strength and pulse width, deterministic SOT field-free switching can be realized. At present, there is no experimental evidence to verify the viability of this scheme. The necessity of an elliptical shape may also limit the application of this scheme. Besides, further investigations should be performed since the FLT of SOT is not included in their simulations.

6. Modulation of HM/FM Interface for Strong DMI

Different spin states will be formed as a competition result among Dzyaloshinskii–Moriya interaction, Heisenberg interaction, dipolar interactions, and Zeeman energy. The interfacial Dzyaloshinskii–Moriya interaction is closely related to the prospect of superior DW dynamics and the formation of magnetic skyrmions. As an emerging topologically protected swirling spin configuration, skyrmion is promising for nonvolatile data storage with high density and low power consumption. Combing the skyrmion with MTJ for skyrmion-based racetrack memory is promising to realize the application of skyrmion on MRAM. The DMI plays an important role in inducing and stabilizing room-temperature isolate chiral skyrmions.

6.1. Origin of DMI

Dzyaloshinskii–Moriya Interaction is named after two scientists Dzyaloshinskii and Moriya, who discovered this phenomenon in 1958[233] and 1960,[234] respectively. DMI in structures with broken inversion symmetry has attracted considerable interest worldwide. As one of the key parts in the creation of magnetic skyrmions and chiral DWs, DMI exhibits a high research value for the next generation of high-speed magnetic storage devices, and a large number of studies on DMI have been reported in recent years.[9,235–237]

The DMI effect can be regarded as an effective field H_{DMI}, which takes the form of $H_{DMI} = (\boldsymbol{S}_1 \times \boldsymbol{S}_2) \cdot \boldsymbol{S}_{12}$. The $\boldsymbol{S}_1$ and $\boldsymbol{S}_2$ are neighboring spins at site 1 and site 2, respectively, $\boldsymbol{d}_{12}$ is the corresponding Dzyaloshinskii–Moriya vector. Apart from the bulk DMI in bulk chiral magnet, the existence of SOC and inversion symmetry breaking at material interfaces will induce an interfacial DMI. As shown in **Figure 19**, when it comes to the interfacial DMI, $\boldsymbol{d}_{12}$ can be written as $\boldsymbol{d}_{12} = d_{12} \cdot (\boldsymbol{z} \cdot \boldsymbol{u}_{12})$,[147] where both $\boldsymbol{z}$ and $\boldsymbol{u}_{12}$ are unit vectors, while $\boldsymbol{z}$ points to the perpendicular direction of the film surface and $\boldsymbol{u}_{12}$ points from site 1 to site 2. For $d_{12} > 0$, the DMI favors anticlockwise rotations from $\boldsymbol{S}_1$ to $\boldsymbol{S}_2$. On the contrary, lower energy for clockwise magnetization rotation corresponds to $d_{12} < 0$. The sign of DMI directly influences the chirality of spin configuration. Using ab initio calculation, DMI energy can be theoretically computed, and more details will be discussed in Section 6.3.

6.2. DW and Skyrmion Motion Induced by DMI and SOT

A domain wall is the boundary region between domains with oppositely aligned magnetization. DW motion has always

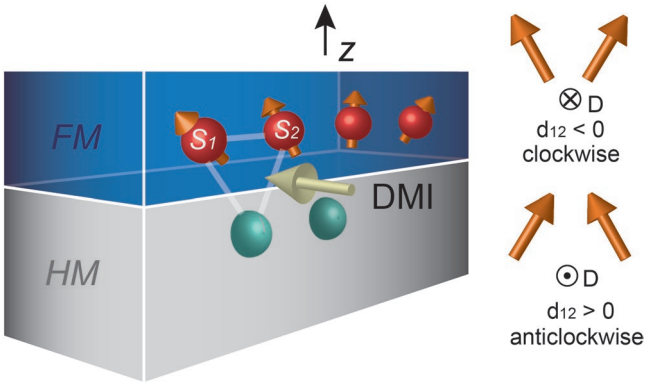

Figure 19. A schematic of DMI induced at the HM/FM interface.

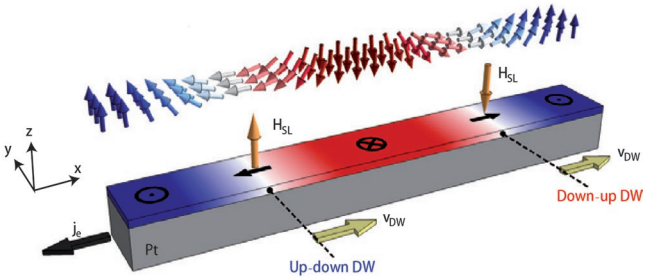

Figure 20. Schematic of DMI-induced chiral DWs. Reproduced with permission.[174] Copyright 2013, Nature Publishing Group.

been a hot topic because of its critical role in magnetization switching, logic implementation, and related applications,[238,239] especially the application possibility in RM.[12]

RM is a new mass storage scheme, in which data bits flow along a nanotrack, thus no mechanical parts are needed. The first RM, proposed in 2008, is DW-RM, where information is encoded by a train of up or down magnetic domains separated by DWs.[12] By injecting an in-plane current into the FM layer, DWs with different polarities obtain the same speed due to Zhang-Li torque,[240] so the width of each domain can be maintained and readout errors can be avoided, which is superior to the field-driven case.

However, the driving current density in this scheme is unbearable, especially when a fast data access rate is required.[12,241] SOT provides a new choice. In 2010, Miron et al. experimentally demonstrated DW motion induced by SOT with a speed as high as 400 m s^{-1}.[182] Note that the DW in this experiment is Bloch-type, which cannot be moved by pure SOT current as the magnetization in the DW is collinear with the electron polarization direction $\boldsymbol{\sigma}$, making both τ^{DL} and τ^{FL} equal to zero. Therefore, an in-plane field is also necessary on this occasion, by the effect of which the magnetization in the DW is partially titled along the x direction, hence nonzero SOT can be obtained. However, as mentioned before, this external field must be removed from an application perspective. In comparison, DMI induced Néel-type DW outperforms Bloch-type DW in this case because its magnetization aligns transversely with $\boldsymbol{\sigma}$. Consequently, the SOT acting on Néel DW maximizes, so the in-plane field is no longer necessary. Meanwhile, moving velocity is improved, making Néel DW a promising candidate in DW-RM. In 2012, Thiaville et al. theoretically studied a new type of Néel DW in a thin film system by adding an additional exchange interaction term, interfacial DMI.[242] In 2013, highly efficient DW motion induced by sole SOT was first evidenced by Beach and co-workers in Pt/Co system, where chiral DW exists due to the large interfacial DMI,[174] as shown in **Figure 20**. Similar results were also obtained in Pt/Co/Ni/Co by Ryu et al.[175]

Magnetic skyrmion is another promising spin component related to DMI. As a type of swirling topological configurations, skyrmions are superior to DWs thanks to the smaller size and lower depinning current density, hence skyrmions are expected to replace DWs as new information carriers in RM.[10,243] Since skyrmions can somewhat be regarded as a superposition of two bending DWs, they can be efficiently driven by SOT, as demonstrated in experiments.[176] However, when driven by a current, skyrmions will gain a velocity toward the edge while moving along the nanotrack, which may cause the annihilation of skyrmions and limit their velocity to ≈100 m s^{-1}.[244,245] This phenomenon, named as skyrmion Hall effect, is an obstacle of skyrmion-based RM. Several methods, such as antiferromagnetically coupled bilayer system[246] and skyrmionium,[247] have been proposed to eliminate it.

6.3. Calculation and Characterization of DMI

To unveil the physical mechanism of DMI and compare different materials, Yang et al. adopted ab initio calculation to obtain theoretical DMI strength.[147,248] Based on the density functional theory, the clockwise energy E_{CW} and the anticlockwise energy E_{ACW} for spin configurations with opposite chirality are first computed. The total DMI strenghth d^{tot} can be introduced by $d^{tot} = (E_{CW} - E_{ACW})/12$. Furthermore, the micro magnetic energy per unit volume is written as $D^{tot} = \frac{3\sqrt{2}d^{tot}}{2N_F r^2}$, where r is the distance between two nearest neighbor Co atoms and N_F is the number of the Co atomic layers.[147]

There are also lots of experimental methods that can be used to characterize the interfacial DMI. The influence of DMI on spin wave dispersion has been theoretically predicted and experimentally demonstrated in an Fe double layer grown on W (110). In 2013, Cortés-Ortuño et al. reported that the DMI would influence the dispersion of spin wave for various crystal symmetries.[249] Later in the same year, Moon et al.[250] deduced a quantitative measurement of DMI energy by comparing the analytical equation with micromagnetic simulation of the asymmetric spin wave propagation in a ferromagnetic/nonmagnet bilayer. These theoretical studies laid the foundation of experimental work to quantify DMI in such a magnetic nanostructure using the Brillouin light spectroscopy (BLS), which is regarded as the most accurate method for DMI value measurement. BLS is ideally tailored for studying the DMI of Pt/FM multilayers thanks to its sub-GHz resolution and few nm surface sensitivities.[251] The mechanism of DMI measurement using BLS setup is depicted in **Figure 21**. Hrabec et al. carried out some measurements on samples with different SiO_2 substrate thickness,[252] which can be conducive to choosing appropriate substrate to enhance the BLS signal. With the propagation of spin wave, all-electrical methods are also a possible way to

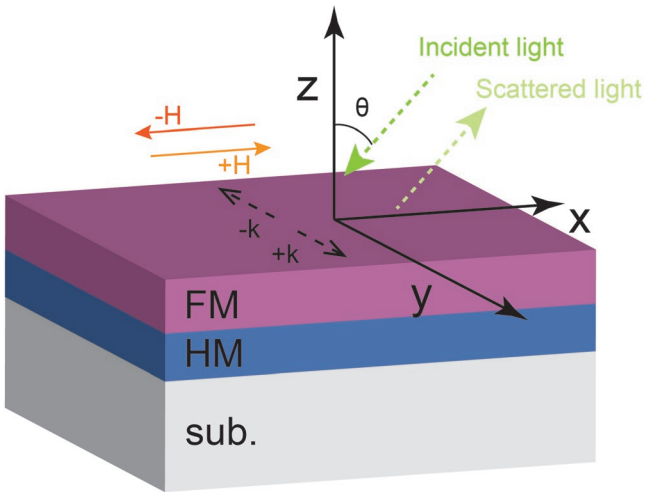

Figure 21. Schematic of the BLS measurement geometry.

measure DMI.[253] The spin-polarized electron energy loss spectroscopy obtained by the momentum-resolved spin dynamics measurement techniques can be used to trace the evidence of DMI,[254] as well as the inelastic neutron scattering.[255] But they are not suitable for multilayers with a top capping layer, therefore they are not widely used.[256]

The visual method to characterize DMI can be realized by a Kerr microscope. The asymmetric DW motions in the creep regime are observed when a perpendicular driven field H_z and an in-plane compensated field H_x are applied.[257,258] In samples with PMA and strong DMI, the magnetization in the center of DW is fixed in a chiral direction by the effective DMI field H_{DMI}, i.e., DW configurations tend to be Néel-type. The presence of an in-plane field will break this configuration, thus affecting the surface energy of DWs and facilitating the DW to be Bloch-type. This change will further influence the field driven DW velocity in the creep regime. To minimize the DW velocity, an in-plane field is expected to reach the same value as H_{DMI}. The energy of DMI can be calculated according to $D = \mu_0 H_{DMI} M_s \sqrt{A / K_{eff}}$. Notice that the direction of the magnetic fields should be carefully calibrated before each start, since the DW velocity will be exponentially influenced by the perpendicular field H_Z with $v \approx \exp\left(-\alpha H_z^{-\frac{1}{4}}\right)$ based on creep scaling law. This is a quite easy access to the DMI information of thin film samples. Although the results in creep regime are usually different from the DMI measured by BLS, the measurement conducted in flow regime seems to be more reliable.[259]

The third type of method to characterize DMI is related to asymmetric hysteresis loops. Interfacial DMI together with an in-plane field creates the shift in magnetic hysteresis of the etched symmetric triangle array on the samples. A robust value and sign of interfacial DMI can be obtained according to these loops, more details can be found in ref. [260]. Another method is based on AHE and SOT+DMI scenario, where an in-plane field H_x is applied to compete with effective DMI field. From the measured hysteresis loop, the current-induced magnetization switching can be spotted with the estimations of DMI obtained in this way.[261] The disadvantage of these methods is that the samples need to be micro and nano fabricated no matter with or without the assistance of current.

6.4. Modulation of DMI

Strong DMI facilitates the formation of chiral spin configurations, and in this way, tuning of DMI is appealing to the stable skyrmions at room temperature. Modulations of DMI in three types of structures are introduced below.

6.4.1. DMI in Pt/Co/HM Structure

HM/FM interface is one of the most typical structures to generate strong DMI because of the strong SOC of heavy metal and ferromagnetic layer. The relative positions of the 3d states in the magnetic metal and the 5d states in the heavy metal are of great importance, as they control the interfacial hybridization and the charge transfer between 3d and 5d states. Pt/Co interface has been intensively investigated in recent years. In 2013, Je et al. showed that the DMI strength in Pt/Co/Pt system is deduced by the symmetric interfaces.[257] Although the thickness difference between the top and bottom Pt layers leads to the structure asymmetry which enhances DMI, it is still not determinant. Other metals like Ir and Pb inducing opposite chirality of DMI with Co comparing to Pt are considered. It has been calculated that inserting Co between Pt and Ir in the trilayer Pt/Co/Ir processes a 15% increment of DMI with respect to Co/Pt bilayers.[248] As the degree of interfacial inversion asymmetry increases, the energy of the DMI is also expected to strengthen.

Due to the considerable DMI energy at both Pt/Co and Ir/Co interfaces, Pt/Co/Ir is a favorable structure to be researched for opposite DMI chiralities. Hrabec et al. compared the differences of DMI between the Pt/Co/Pt and Pt/Co/Ir/Pt systems and explored the changes of DMI by varying Ir thickness.[262] Shahbazi et al. also changed the thickness of Ir in Pt/Co/Ir/Ta multilayers to observe DW motion.[263]

6.4.2. DMI in Pt/Co/MgO Structure

Pt/Co/MgO multilayers are similar to the configuration of the tunnel barrier layer/free layer/capping layer, which is one of the most popular MTJ structures. Therefore, it is possible to investigate the DMI effects including the electrical nucleation and detection of magnetic skyrmions in MTJs with HM/FM/metal oxide stack. Apart from Co, the MgO layer at the interfaces could also be used for fine-tuning the DMI in Pt/Co/MgO samples, which is valuable for the induction of chiral magnetic order.

Different from three-site interaction which exists at HM/FM interface, designing multilayers with oxide is not only an efficient method to enhance DMI, but also a base for electrical detection of skyrmions in spintronic devices. It was also calculated that DMI is enhanced by 60% in

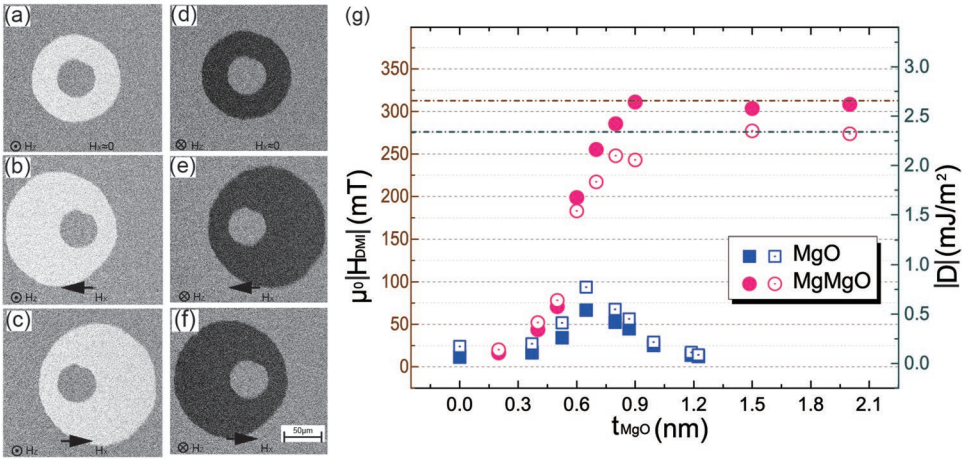

Figure 22. DW expansion of Pt/Co/Mg/MgO(0.6 nm) multilayers driven by a,d) an out-of-plane magnetic field $\mu_0|H_Z| = 8$ mT with an in-plane field $\mu_0|H_x|$ approximately 0, b,c,e,f) with $\mu_0|H_Z| = 327$ mT. Field directions have been marked in each image. Images in (a)–(f) were obtained by subtracting four images with a specific time interval from a background with no DW. All images of DW were captured using Kerr microscopy. g) Trends of the effective DMI field and DMI constant as a function of t_{MgO}. Square symbols represent Pt/Co/MgO (t_{MgO}) samples while circular symbols represent Pt/Co/Mg/MgO(t_{MgO}). Closed symbols represent $\mu_0|H_{DMI}|$ and open symbols represent $|D|$.[258] Reproduced with permission.[258] Copyright 2018, Royal Society of Chemistry.

oxide/Co/Pt structures compared to Co/Pt bilayers.[248] According to density functional theory calculation, a large charge transfer and a strong interfacial electric field are induced at the oxide/Co interface, and they might compensate the small SOC of the interfacial atoms.[241,264–266]

A method to control DMI by changing the thickness of MgO layer t_{MgO} in Pt/Co/oxide system was reported in 2018.[258] Kerr microscope was adopted to observe asymmetric DW motions with both perpendicular and in-plane magnetic fields, as shown in **Figure 22**a–f. In a DMI dominated multilayer structure, varying the thickness of oxide layer seems ineffective on the DMI constant $|D|$ of the whole structure. Surprisingly, a nonlinear trend of DMI is observed in Pt/Co/MgO multilayers. After inserting a dust of Mg between the Co/MgO interface, the strength of DMI is prominently enhanced by 5 times. With the increment of t_{MgO}, DMI constant first increases and then saturates at 2.32 mJ m^{-2}. The trends of the effective DMI field and DMI constant are depicted in Figure 22g.

On the one hand, as MgO becomes thicker, the number of Co—O bonds at Co/MgO interface increases, directly resulting in an increment of $|D|$. On the other hand, Co will be intensively deteriorated with diffused O atoms. The following decrement for Pt/Co/MgO structure is also coordinated with the trends of $|D|$ for Pt/Co/Mg/MgO structure. With the protection of an ultrathin Mg layer, Co atoms can integrate with O atoms to the maximum when t_{MgO} increases.

6.4.3. DMI in HM/CoFeB/MgO Structure

As one of the most popular structures of MTJs, CoFeB/MgO systems are discussed in this part. Compared with Co systems mentioned above, CoFeB is slightly inferior in inducing strong DMI and there are more possibilities influencing interfacial DMI, such as the diffusion of B atoms.[267] Groups of researchers have been interested in the DMI of CoFeB/MgO structures. Torrejon et al. and Gross et al. controlled the magnetic chirality as well as interfacial DMI by changing heavy metals in HM/CoFeB/MgO heterostructures.[65,268] The results proved that the strength of DMI is related to the filling of 5d orbitals, or the electronegativity of the heavy metal layer. Compared with samples based on Hf, Ta, and TaN, samples with underlayer of W show the strongest DMI, as shown in **Figure 23**.

Besides, thermal annealing is found to be helpful for enhancing DMI in Ta/CoFeB/MgO trilayers, but temperature above a specific value would damage this effect.[269] In addition, room-temperature skyrmions are observed in W/CoFeB/MgO thin films and microwires, and they cannot exist stably without interfacial DMI.[264]

7. Outlook

In this review, we described the modulation of the HM/FM interface for high-performance spintronic devices. The properties such as PMA, TMR, magnetic damping, SOT switching, and DMI were covered. It was demonstrated that the HM/FM interface can generate magnetic anisotropy and influence the TMR effect. By exploiting the double-interface structure and choosing proper spacer layer material (e.g., W), the interfacial PMA and TMR ratio can be significantly increased, conducive to the enhancement of thermal stability and reduction of read error rate. In STT-based magnetization switching, a low magnetic damping constant is required for low-power writing operations. The W-based structure exhibits much lower magnetic damping constant than that of the Ta-based counterpart, leading to smaller STT switching current. As for the SOT switching, β-W/CoFeB/MgO structure is adopted as β-W gives rise to relatively large spin Hall angle. Antiferromagnetic materials (e.g., IrMn) and TIs (e.g., $(Bi_{0.5}Sb_{0.5})_2Te_3$) are also widely explored due to the potential of achieving

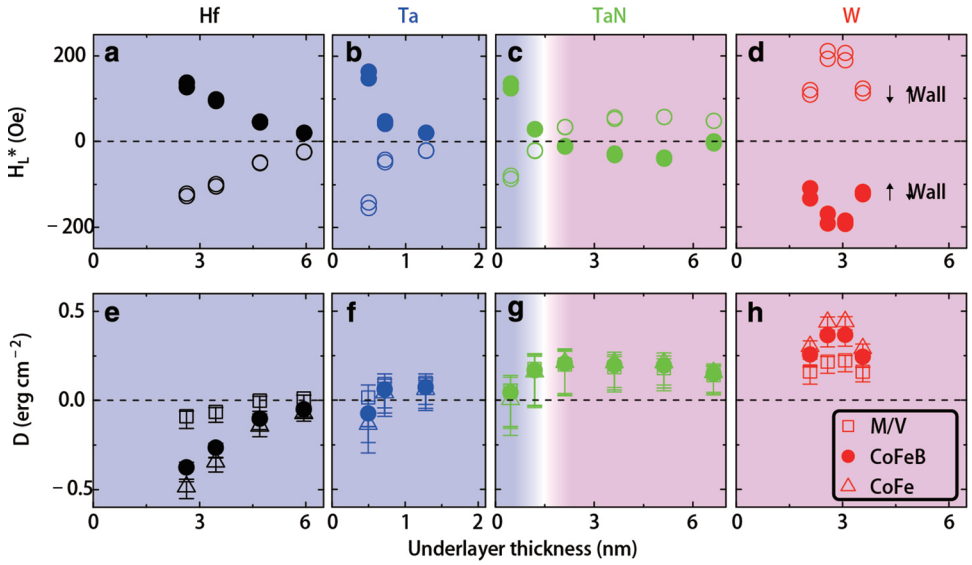

Figure 23. Underlayer-dependent Dzyaloshinskii–Moriya interaction. Reproduced with permission.[65] Copyright 2014, Nature Publishing Group.

field-free SOT switching and giant spin Hall angle. Besides, by adjusting the HM/FM interface, the DMI can be effectively regulated, which is essential for DW dynamics and magnetic skyrmions.

Rapid development of spintronic devices in the past decades has laid a solid foundation for emerging applications. For instance, in 2015, STT-MRAM with capacity of 1 Gbit was presented with 40–50 nm perpendicularly magnetized MTJs.[270] Later in 2016, Chung et al. demonstrated 4 Gbit STT-MRAM with cell projection area of $9F^2$.[271] Nevertheless, there are many remaining questions and novel areas to be explored. First, as MTJ size shrinks down to 10 nm, thermal stability factor reduces to smaller than 25,[92,95] which is insufficient for nonvolatile memory. Innovative HM materials (e.g., Bi) and FM materials with bulk PMA (e.g., MnGa) may be utilized to solve this problem.[79,272] Besides, MTJ with shape anisotropy was demonstrated to possess sufficient thermal stability with junction size smaller than 10 nm,[273,274] which may be another direction for STT-MRAMs. Second, continuous efforts have been devoted to lowering read error rate. Though TMR ratio of 249% is obtained in atom-thick W engineered MTJs,[101] high TMR ratio is urgently needed by industry.[275] Recent theoretical studies have predicted high TMR ratio by utilizing novel FM materials or 2D materials,[276–278] which needs to be verified through experiments. Besides, STT and SOT switching still suffer from large switching current. This problem may be solved by employing the interplay of SOT and STT, or utilizing the voltage-assisted SOT.[188,279–283] Finally, strong DMI is required for skyrmion applications, which relies on material progress and novel phenomena such as voltage-control of DMI.

The investigations of HM/FM interface have opened up such a broad perspective that modulation of this interface will have a substantial and continuous effect on device performances. With extensive academic and industrial efforts into spintronic devices, more developments and commercial applications can be expected in the near future.

Acknowledgements

S.P., D.Z., and J.Z. contributed equally to this work. The authors thank the National Natural Science Foundation of China (Grant Nos. 61627813 and 61571023), the International Collaboration Project B16001, the National Key Technology Program of China 2017ZX01032101, the VR innovation platform from Qingdao Science and Technology Commission, and the Magnetic Sensor platform from Laoshan District for their financial support of this work.

Conflict of Interest

The authors declare no conflict of interest.

Keywords

Dzyaloshinskii–Moriya interaction, heavy metal/ferromagnetic metal interface, perpendicular magnetic anisotropy, spin–orbit torque, spintronics

Received: January 31, 2019
Revised: April 18, 2019
Published online:

[1] M. N. Baibich, J. M. Broto, A. Fert, F. Nguyen Van Dau, F. Petroff, P. Eitenne, G. Creuzet, A. Friederich, J. Chazelas, *Phys. Rev. Lett.* **1988**, *61*, 2472.
[2] G. Binasch, P. Grünberg, F. Saurenbach, W. Zinn, *Phys. Rev. B* **1989**, *39*, 4828.
[3] J. A. Katine, F. J. Albert, R. A. Buhrman, E. B. Myers, D. C. Ralph, *Phys. Rev. Lett.* **2000**, *84*, 3149.
[4] I. M. Miron, G. Gaudin, S. Auffret, B. Rodmacq, A. Schuhl, S. Pizzini, J. Vogel, P. Gambardella, *Nat. Mater.* **2010**, *9*, 230.
[5] I. M. Miron, K. Garello, G. Gaudin, P.-J. Zermatten, M. V. Costache, S. Auffret, S. Bandiera, B. Rodmacq, A. Schuhl, P. Gambardella, *Nature* **2011**, *476*, 189.

[6] L. Liu, C.-F. Pai, Y. Li, H. W. Tseng, D. C. Ralph, R. A. Buhrman, *Science* **2012**, *336*, 555.
[7] M. Julliere, *Phys. Lett. A* **1975**, *54*, 225.
[8] S. Mühlbauer, B. Binz, F. Jonietz, C. Pfleiderer, A. Rosch, A. Neubauer, R. Georgii, P. Böni, *Science* **2011**, *323*, 914.
[9] X. Z. Yu, Y. Onose, N. Kanazawa, J. H. Park, J. H. Han, Y. Matsui, N. Nagaosa, Y. Tokura, *Nature* **2010**, *465*, 901.
[10] F. C. Vincent, S. Joao, *Nat. Nanotechnol.* **2013**, *8*, 152.
[11] W. Kang, Y. Huang, X. Zhang, Y. Zhou, W. Zhao, *Proc. IEEE* **2016**, *104*, 2040.
[12] S. S. P. Parkin, M. Hayashi, L. Thomas, *Science* **2008**, *320*, 190.
[13] M. Hayashi, L. Thomas, R. Moriya, C. Rettner, S. S. P. Parkin, *Science* **2008**, *320*, 209.
[14] S. S. P. Parkin, C. Kaiser, A. Panchula, P. M. Rice, B. Hughes, M. Samant, S. Yang, *Nat. Mater.* **2004**, *3*, 862.
[15] S. Yuasa, T. Nagahama, A. Fukushima, Y. Suzuki, K. Ando, *Nat. Mater.* **2004**, *3*, 868.
[16] B. Dieny, M. Chshiev, *Rev. Mod. Phys.* **2017**, *89*, 025008.
[17] G.-G. An, J.-B. Lee, S.-M. Yang, J.-H. Kim, W.-S. Chung, J.-P. Hong, *Acta Mater.* **2015**, *87*, 259.
[18] S.-E. Lee, T.-H. Shim, J.-G. Park, *NPG Asia Mater.* **2016**, *8*, e324.
[19] J.-M. Hu, Z. Li, L.-Q. Chen, C.-W. Nan, *Nat. Commun.* **2011**, *2*, 553.
[20] K. L. Wang, J. G. Alzate, P. K. Amiri, *J. Phys. D: Appl. Phys.* **2013**, *46*, 074003.
[21] A. D. Kent, D. C. Worledge, *Nat. Nanotechnol.* **2015**, *10*, 187.
[22] P. F. Carcia, A. D. Meinhaldt, A. Suna, *Appl. Phys. Lett.* **1985**, *47*, 178.
[23] P. F. Carcia, *J. Appl. Phys.* **1988**, *63*, 5066.
[24] S. Hashimoto, Y. Ochiai, K. Aso, *J. Appl. Phys.* **1989**, *66*, 4909.
[25] J. H. Park, C. Park, T. Jeong, M. T. Moneck, N. T. Nufer, J. G. Zhu, *J. Appl. Phys.* **2008**, *103*, 07A917.
[26] D. Lim, K. Kim, S. Kim, W. Y. Jeung, S. R. Lee, *IEEE Trans. Magn.* **2009**, *45*, 2407.
[27] K. Yakushiji, T. Saruya, H. Kubota, A. Fukushima, T. Nagahama, S. Yuasa, K. Ando, *Appl. Phys. Lett.* **2010**, *97*, 232508.
[28] M. Gottwald, J. J. Kan, K. Lee, X. Zhu, C. Park, S. H. Kang, *Appl. Phys. Lett.* **2015**, *106*, 032413.
[29] K. Yakushiji, H. Kubota, A. Fukushima, S. Yuasa, *Appl. Phys. Express* **2015**, *8*, 083003.
[30] K. Yakushiji, A. Sugihara, A. Fukushima, H. Kubota, S. Yuasa, *Appl. Phys. Lett.* **2017**, *110*, 092406.
[31] S. Andrieu, T. Hauet, M. Gottwald, A. Rajanikanth, L. Calmels, A. M. Bataille, F. Montaigne, S. Mangin, E. Otero, P. Ohresser, P. Le Fèvre, F. Bertran, A. Resta, A. Vlad, A. Coati, Y. Garreau, *Phys. Rev. Mater.* **2018**, *2*, 064410.
[32] J. M. L. Beaujour, W. Chen, K. Krycka, C. C. Kao, J. Z. Sun, A. D. Kent, *Eur. Phys. J. B* **2007**, *59*, 475.
[33] G. H. O. Daalderop, P. J. Kelly, F. J. A. Den Broeder, *Phys. Rev. Lett.* **1992**, *68*, 682.
[34] M. Gottwald, S. Andrieu, F. Gimbert, E. Shipton, L. Calmels, C. Magen, E. Snoeck, M. Liberati, T. Hauet, E. Arenholz, S. Mangin, E. E. Fullerton, *Phys. Rev. B* **2012**, *86*, 014425.
[35] S. Girod, M. Gottwald, S. Andrieu, S. Mangin, J. McCord, E. E. Fullerton, J.-M. L. Beaujour, B. J. Krishnatreya, A. D. Kent, *Appl. Phys. Lett.* **2009**, *94*, 262504.
[36] L. You, R. C. Sousa, S. Bandiera, B. Rodmacq, B. Dieny, *Appl. Phys. Lett.* **2012**, *100*, 172411.
[37] G. S. Kar, W. Kim, T. Tahmasebi, J. Swerts, S. Mertens, N. Heylen, T. Min, *IEEE Int. Electron Devices Meet.* **2014**, *19*, 1.
[38] S. Ikeda, K. Miura, H. Yamamoto, K. Mizunuma, H. D. Gan, M. Endo, S. Kanai, J. Hayakawa, F. Matsukura, H. Ohno, *Nat. Mater.* **2010**, *9*, 721.
[39] M. T. Johnson, P. J. H. Bloemen, F. J. A. Broeder, J. J. Vries, *Rep. Prog. Phys.* **1996**, *59*, 11.
[40] M. K. Niranjan, C. G. Duan, S. S. Jaswal, E. Y. Tsymbal, *Appl. Phys. Lett.* **2010**, *96*, 222504.
[41] H. X. Yang, M. Chshiev, B. Dieny, J. H. Lee, A. Manchon, K. H. Shin, *Phys. Rev. B* **2011**, *84*, 054401.
[42] A. Hallal, H. X. Yang, B. Dieny, M. Chshiev, *Phys. Rev. B* **2013**, *88*, 184423.
[43] S. Peng, W. Kang, M. Wang, K. Cao, X. Zhao, L. Wang, Y. Zhang, Y. Zhang, Y. Zhou, K. L. Wang, W. Zhao, *IEEE Magn. Lett.* **2017**, *8*, 3105805.
[44] J. M. Slaughter, K. Nagel, R. Whig, S. Deshpande, S. Aggarwal, M. Deherrera, J. Janesky, M. Lin, H. Chia, *IEEE Int. Electron Devices Meet.* **2016**, *21*, 5.
[45] W. Zhao, Y. Zhang, T. Devolder, J. O. Klein, D. Ravelosona, C. Chappert, P. Mazoyer, *Microelectron. Reliab.* **2012**, *52*, 1848.
[46] R. Takemura, T. Kawahara, K. Miura, H. Yamamoto, J. Hayakawa, N. Matsuzaki, K. Ono, M. Yamanouchi, K. Ito, H. Takahashi, S. Ikeda, H. Hasegawa, H. Matsuoka, H. Ohno, *IEEE J. Solid-State Circuits* **2010**, *45*, 869.
[47] D. C. Worledge, G. Hu, D. W. Abraham, J. Z. Sun, P. L. Trouilloud, J. Nowak, S. Brown, M. C. Gaidis, E. J. O'Sullivan, R. P. Robertazzi, *Appl. Phys. Lett.* **2011**, *98*, 022501.
[48] W. X. Wang, Y. Yang, H. Naganuma, Y. Ando, R. C. Yu, X. F. Han, *Appl. Phys. Lett.* **2011**, *99*, 4.
[49] N. Miyakawa, D. C. Worledge, K. Kita, *IEEE Magn. Lett.* **2013**, *4*, 1000104.
[50] H. Meng, R. Sbiaa, C. C. Wang, S. Y. H. Lua, A. K. Akhtar, *J. Appl. Phys.* **2011**, *110*, 103915.
[51] C. W. Cheng, W. Feng, G. Chern, C. M. Lee, T. H. Wu, *J. Appl. Phys.* **2011**, *110*, 033916.
[52] J. Sinha, M. Hayashi, A. J. Kellock, S. Fukami, M. Yamanouchi, H. Sato, S. Ikeda, S. Mitani, S. Yang, S. S. P. Parkin, H. Ohno, *Appl. Phys. Lett.* **2013**, *102*, 242405.
[53] V. Sokalski, M. T. Moneck, E. Yang, J.-G. Zhu, *Appl. Phys. Lett.* **2012**, *101*, 072411.
[54] T.-I. Cheng, C.-W. Cheng, G. Chern, *J. Appl. Phys.* **2012**, *112*, 033910.
[55] J. Kim, J. Sinha, M. Hayashi, M. Yamanouchi, S. Fukami, T. Suzuki, S. Mitani, H. Ohno, *Nat. Mater.* **2013**, *12*, 240.
[56] J. Sinha, M. Gruber, M. Kodzuka, T. Ohkubo, S. Mitani, K. Hono, M. Hayashi, *J. Appl. Phys.* **2015**, *117*, 043913.
[57] S. Yang, J. Lee, G. An, J. Kim, W. Chung, J. Hong, *Thin Solid Films* **2015**, *587*, 39.
[58] A. A. Greer, A. X. Gray, S. Kanai, A. M. Kaiser, S. Ueda, Y. Yamashita, C. Bordel, G. Palsson, N. Maejima, S.-H. Yang, G. Conti, K. Kobayashi, S. Ikeda, F. Matsukura, H. Ohno, C. M. Schneider, J. B. Kortright, F. Hellman, C. S. Fadley, *Appl. Phys. Lett.* **2012**, *101*, 202402.
[59] Z. Wang, M. Saito, K. P. McKenna, S. Fukami, H. Sato, S. Ikeda, H. Ohno, Y. Ikuhara, *Nano Lett.* **2016**, *16*, 1530.
[60] S. Mukherjee, R. Knut, S. M. Mohseni, T. N. Anh Nguyen, S. Chung, Q. Tuan Le, J. Åkerman, J. Persson, A. Sahoo, A. Hazarika, B. Pal, S. Thiess, M. Gorgoi, P. S. A. Kumar, W. Drube, O. Karis, D. D. Sarma, *Phys. Rev. B* **2015**, *91*, 085311.
[61] T. Liu, J. W. Cai, L. Sun, *AIP Adv.* **2012**, *2*, 032151.
[62] C.-F. Pai, M.-H. Nguyen, C. Belvin, L. H. Vilela-Leão, D. C. Ralph, R. A. Buhrman, *Appl. Phys. Lett.* **2014**, *104*, 082407.
[63] D.-S. Lee, H.-T. Chang, C.-W. Cheng, G. Chern, *IEEE Trans. Magn.* **2014**, *50*, 3201904.
[64] W. Skowroński, T. Nozaki, Y. Shiota, S. Tamaru, K. Yakushiji, H. Kubota, A. Fukushima, S. Yuasa, Y. Suzuki, *Appl. Phys. Express* **2015**, *8*, 053003.
[65] J. Torrejon, J. Kim, J. Sinha, S. Mitani, M. Hayashi, M. Yamanouchi, H. Ohno, *Nat. Commun.* **2014**, *5*, 4655.
[66] B. Cui, C. Song, G. Y. Wang, Y. Y. Wang, F. Zeng, F. Pan, *J. Alloys Compd.* **2013**, *559*, 112.

[67] C.-H. Lambert, A. Rajanikanth, T. Hauet, S. Mangin, E. E. Fullerton, S. Andrieu, *Appl. Phys. Lett.* **2013**, *102*, 122410.
[68] Y.-W. Oh, K.-D. Lee, J.-R. Jeong, B.-G. Park, *J. Appl. Phys.* **2014**, *115*, 17C724.
[69] P. J. Chen, Y. L. Iunin, S. F. Cheng, R. D. Shull, *IEEE Trans. Magn.* **2016**, *52*, 4400504.
[70] W. Skowroński, T. Nozaki, D. D. Lam, Y. Shiota, K. Yakushiji, H. Kubota, A. Fukushima, S. Yuasa, Y. Suzuki, *Phys. Rev. B* **2015**, *91*, 184410.
[71] T. Liu, Y. Zhang, J. W. Cai, H. Y. Pan, *Sci. Rep.* **2014**, *4*, 5895.
[72] H. Almasi, C. L. Sun, X. Li, T. Newhouse-Illige, C. Bi, K. C. Price, S. Nahar, C. Grezes, Q. Hu, P. K. Amiri, K. L. Wang, P. M. Voyles, W. G. Wang, *J. Appl. Phys.* **2017**, *121*, 153902.
[73] J. Chatterjee, R. C. Sousa, N. Perrissin, S. Auffret, C. Ducruet, B. Dieny, *Appl. Phys. Lett.* **2017**, *110*, 202401.
[74] H. Almasi, D. R. Hickey, T. Newhouse-Illige, M. Xu, M. R. Rosales, S. Nahar, J. T. Held, K. A. Mkhoyan, W. G. Wang, *Appl. Phys. Lett.* **2015**, *106*, 182406.
[75] H. Almasi, M. Xu, Y. Xu, T. Newhouse-Illige, W. G. Wang, *Appl. Phys. Lett.* **2016**, *109*, 032401.
[76] K. Watanabe, S. Fukami, H. Sato, F. Matsukura, H. Ohno, *IEEE Trans. Magn.* **2016**, *52*, 3400904.
[77] Y. Liu, K. Zhu, Z. HuiCai, Z. Zhu, T. Yu, S. Ma, *Chinese Phys. B* **2016**, *25*, 117805.
[78] S. Peng, M. Wang, H. Yang, L. Zeng, J. Nan, J. Zhou, Y. Zhang, A. Hallal, M. Chshiev, K. L. Wang, Q. Zhang, W. Zhao, *Sci. Rep.* **2015**, *5*, 18173.
[79] S. Peng, W. Zhao, J. Qiao, L. Su, J. Zhou, H. Yang, Q. Zhang, Y. Zhang, C. Grezes, P. K. Amiri, K. L. Wang, *Appl. Phys. Lett.* **2017**, *110*, 072403.
[80] S. Peng, L. Wang, X. Li, Z. Wang, J. Zhou, J. Qiao, R. Chen, Y. Zhang, K. L. Wang, W. Zhao, *IEEE Trans. Magn.* **2018**, *54*, 1300705.
[81] Y. Miura, M. Tsujikawa, M. Shirai, *J. Appl. Phys.* **2013**, *113*, 233908.
[82] D. Odkhuu, S. H. Rhim, N. Park, S. C. Hong, *Phys. Rev. B* **2013**, *88*, 184405.
[83] Z. Bai, L. Shen, Y. Cai, Q. Wu, M. Zeng, G. Han, Y. P. Feng, *New J. Phys.* **2014**, *16*, 103033.
[84] A. Hallal, B. Dieny, M. Chshiev, *Phys. Rev. B* **2014**, *90*, 064422.
[85] P. V. Ong, N. Kioussis, D. Odkhuu, P. K. Amiri, K. L. Wang, G. P. Carman, *Phys. Rev. B* **2015**, *92*, 020407.
[86] P. V. Ong, N. Kioussis, P. K. Amiri, K. L. Wang, G. P. Carman, *J. Appl. Phys.* **2015**, *117*, 17B518.
[87] H. Yang, A. D. Vu, A. Hallal, N. Rougemaille, J. Coraux, G. Chen, A. K. Schmid, M. Chshiev, *Nano Lett.* **2016**, *16*, 145.
[88] S. Peng, S. Li, W. Kang, J. Zhou, N. Lei, Y. Zhang, H. Yang, X. Li, P. K. Amiri, K. L. Wang, W. Zhao, *Appl. Phys. Lett.* **2017**, *111*, 152403.
[89] K. Nakamura, T. Nomura, A. M. Pradipto, K. Nawa, T. Akiyama, T. Ito, *J. Magn. Magn. Mater.* **2017**, *429*, 214.
[90] J. Qiao, S. Peng, Y. Zhang, H. Yang, W. Zhao, *Phys. Rev. B* **2018**, *97*, 054420.
[91] H. Sato, M. Yamanouchi, S. Ikeda, S. Fukami, F. Matsukura, H. Ohno, *Appl. Phys. Lett.* **2012**, *101*, 022414.
[92] H. Sato, E. C. I. Enobio, M. Yamanouchi, S. Ikeda, S. Fukami, S. Kanai, F. Matsukura, H. Ohno, *Appl. Phys. Lett.* **2014**, *105*, 062403.
[93] S. Ikeda, H. Sato, H. Honjo, E. C. I. Enobio, S. Ishikawa, M. Yamanouchi, S. Fukami, S. Kanai, F. Matsukura, T. Endoh, H. Ohno, *IEEE Int. Electron Devices Meet.* **2014**, *33*, 2.
[94] H. Sato, M. Yamanouchi, S. Ikeda, S. Fukami, F. Matsukura, H. Ohno, *IEEE Trans. Magn.* **2013**, *49*, 4437.
[95] J.-H. Kim, J.-B. Lee, G.-G. An, S.-M. Yang, W.-S. Chung, H.-S. Park, J.-P. Hong, *Sci. Rep.* **2015**, *5*, 16903.
[96] L. Cuchet, B. Rodmacq, S. Auffret, R. C. Sousa, I. L. Prejbeanu, B. Dieny, *Sci. Rep.* **2016**, *6*, 21246.
[97] S. S. P. Parkin, *Phys. Rev. Lett.* **1991**, *67*, 3598.
[98] S. S. P. Parkin, D. Mauri, *Phys. Rev. B* **1991**, *44*, 7131.
[99] X. Zhang, Y. Zhang, J. W. Cai, *J. Appl. Phys.* **2015**, *118*, 143903.
[100] Y. Huai, H. Gan, Z. Wang, P. Xu, X. Hao, B. K. Yen, R. Malmhall, N. Pakala, C. Wang, J. Zhang, Y. Zhou, D. Jung, K. Satoh, R. Wang, L. Xue, M. Pakala, *Appl. Phys. Lett.* **2018**, *112*, 092402.
[101] M. Wang, W. Cai, K. Cao, J. Zhou, J. Wrona, S. Peng, H. Yang, J. Wei, W. Kang, Y. Zhang, J. Langer, B. Ocker, A. Fert, W. Zhao, *Nat. Commun.* **2018**, *9*, 671.
[102] S. A. Wolf, D. D. Awschalom, R. A. Buhrman, J. M. Daughton, S. von Molnár, M. L. Roukes, A. Y. Chtchelkanova, D. M. Treger, *Science* **2001**, *294*, 1488.
[103] I. Zutić, J. Fabian, S. Das Sarma, *Rev. Mod. Phys.* **2004**, *76*, 323.
[104] T. Miyazaki, N. Tezuka, *J. Magn. Magn. Mater* **1995**, *139*, L231.
[105] J. S. Moodera, L. R. Kinder, T. M. Wong, R. Meservey, *Phys. Rev. Lett.* **1995**, *74*, 3273.
[106] J. Mathon, A. Umerski, *Phys. Rev. B* **2001**, *63*, 220403.
[107] W. H. Butler, X.-G. Zhang, T. C. Schulthess, J. M. MacLaren, *Phys. Rev. B* **2001**, *63*, 054416.
[108] X.-G. Zhang, W. H. Butler, *Phys. Rev. B* **2004**, *70*, 172407.
[109] D. D. Djayaprawira, K. Tsunekawa, M. Nagai, H. Maehara, S. Yamagata, N. Watanabe, S. Yuasa, Y. Suzuki, K. Ando, *Appl. Phys. Lett.* **2005**, *86*, 092502.
[110] S. Ikeda, J. Hayakawa, Y. Ashizawa, Y. M. Lee, K. Miura, H. Hasegawa, M. Tsunoda, F. Matsukura, H. Ohno, *Appl. Phys. Lett.* **2008**, *93*, 082508.
[111] Z. Wang, W. Zhao, E. Deng, J.-O. Klein, C. Chappert, *J. Phys. D: Appl. Phys.* **2015**, *48*, 065001.
[112] C.-F. Pai, L. Liu, Y. Li, H. W. Tseng, D. C. Ralph, R. A. Buhrman, *Appl. Phys. Lett.* **2012**, *101*, 122404.
[113] G. Y. Guo, S. Murakami, T.-W. Chen, N. Nagaosa, *Phys. Rev. Lett.* **2008**, *100*, 096401.
[114] M.-H. Nguyen, C.-F. Pai, K. X. Nguyen, D. A. Muller, D. C. Ralph, R. A. Buhrman, *Appl. Phys. Lett.* **2015**, *106*, 222402.
[115] S. V. Aradhya, G. E. Rowlands, J. Oh, D. C. Ralph, R. A. Buhrman, *Nano Lett.* **2016**, *16*, 5987.
[116] Y. Yang, W. X. Wang, Y. Yao, H. F. Liu, H. Naganuma, T. S. Sakul, X. F. Han, R. C. Yu, *Appl. Phys. Lett.* **2012**, *101*, 012406.
[117] S.-E. Lee, J.-U. Baek, J.-G. Park, *Sci. Rep.* **2017**, *7*, 11907.
[118] H. Meng, W. H. Lum, R. Sbiaa, S. Y. H. Lua, H. K. Tan, *J. Appl. Phys.* **2011**, *110*, 033904.
[119] M.-S. Jeon, K.-S. Chae, D.-Y. Lee, Y. Takemura, S.-E. Lee, T.-H. Shim, J.-G. Park, *Nanoscale* **2015**, *7*, 8142.
[120] H. D. Gan, H. Sato, M. Yamanouchi, S. Ikeda, K. Miura, R. Koizumi, F. Matsukura, H. Ohno, *Appl. Phys. Lett.* **2011**, *99*, 252507.
[121] M. Yamanouchi, R. Koizumi, S. Ikeda, H. Sato, K. Mizunuma, K. Miura, H. D. Gan, F. Matsukura, H. Ohno, *J. Appl. Phys.* **2011**, *109*, 07C712.
[122] B. Fang, X. Zhang, B. S. Zhang, Z. M. Zeng, J. W. Cai, *AIP Adv.* **2015**, *5*, 067116.
[123] H.-C. Chung, Y.-H. Lee, S.-R. Lee, *Phys. Status Solidi A* **2007**, *204*, 3995.
[124] M. Li, J. Lu, G. Yu, X. Li, G. Han, X. Chen, H. Shi, G. Yu, P. K. Amiri, K. L. Wang, *AIP Adv.* **2016**, *6*, 045107.
[125] S.-E. Lee, Y. Takemura, J.-G. Park, *Appl. Phys. Lett.* **2016**, *109*, 182405.
[126] M. Cubukcu, O. Boulle, M. Drouard, K. Garello, C. Onur Avci, I. Mihai Miron, J. Langer, B. Ocker, P. Gambardella, G. Gaudin, *Appl. Phys. Lett.* **2014**, *104*, 042406.
[127] M. Cubukcu, O. Boulle, N. Mikuszeit, C. Hamelin, T. Brcher, N. Lamard, M. Cyrille, L. BudaPrejbeanu, K. Garello, I. M. Miron,

O. Klein, G. de Loubens, V. V. Naletov, J. Langer, B. Ocker, P. Gambardella, G. Gaudin, *IEEE Trans. Magn.* **2018**, *54*, 1.
[128] M. Bapna, B. Parks, S. D. Oberdick, H. Almasi, W. Wang, S. A. Majetich, *Phys. Rev. Appl.* **2018**, *10*, 024013.
[129] B. Taudul, E. N. Monteblanco, U. Halisdemir, D. Lacour, F. Schleicher, F. Montaigne, E. Beaurepaire, S. Boukari, M. Hehn, M. Alouani, M. Bowen, *Adv. Electron. Mater.* **2016**, *3*, 1600390.
[130] J. Zhang, C. Franz, M. Czerner, C. Heiliger, *Phys. Rev. B* **2014**, *90*, 184409.
[131] J. Zhou, W. Zhao, S. Peng, J. Qiao, J. Klein, X. Lin, Y. Zhang, A. Bournel, *IEEE Tran. Magn.* **2017**, *53*, 1.
[132] J. Zhou, W. Zhao, Y. Wang, S. Peng, J. Qiao, L. Su, L. Zeng, N. Lei, L. Liu, Y. Zhang, A. Bournel, *Appl. Phys. Lett.* **2016**, *109*, 242403.
[133] K. Sankaran, J. Swerts, S. Couet, K. Stokbro, G. Pourtois, *Phys. Rev. B* **2016**, *94*, 094424.
[134] M. Benakli, A. F. Torabi, M. L. Mallary, H. Zhou, H. N. Bertram, *IEEE Trans. Magn.* **2001**, *37*, 1564.
[135] D. Lacour, J. A. Katine, N. Smith, M. J. Carey, J. R. Childress, *Appl. Phys. Lett.* **2004**, *85*, 4681.
[136] Y. Zhao, Q. Song, S. H. Yang, T. Su, W. Yuan, S. S. P. Parkin, J. Shi, W. Han, *Sci. Rep.* **2016**, *6*, 22890.
[137] S. Mizukami, Y. Ando, T. Miyazaki, *J. Magn. Magn. Mater.* **2001**, *226*, 1640.
[138] D. Bastian, E. Biller, *Phys. Status Solidi A* **1976**, *35*, 113.
[139] V. Kamberský, *Can. J. Phys.* **1970**, *48*, 2906.
[140] Y. Tserkovnyak, A. Brataas, G. E. W. Bauer, *Phys. Rev. Lett.* **2002**, *88*, 117601.
[141] W. Zhao, X. Zhao, B. Zhang, K. Cao, L. Wang, W. Kang, Q. Shi, M. Wang, Y. Zhang, Y. Wang, S. Peng, J.-O. Klein, L. A. de Barros Naviner, D. Ravelosona, *Materials* **2016**, *9*, 41.
[142] S. Woo, M. Mann, A. J. Tan, L. Caretta, G. S. D. Beach, *Appl. Phys. Lett.* **2014**, *105*, 212404.
[143] K. F. Huang, D. S. Wang, H. H. Lin, C. H. Lai, *Appl. Phys. Lett.* **2015**, *107*, 232407.
[144] A. van den Brink, G. Vermijs, A. Solignac, J. Koo, J. T. Kohlhepp, H. J. M. Swagten, B. Koopmans, *Nat. Commun.* **2016**, *7*, 10854.
[145] I. M. Miron, P. J. Zermatten, G. Gaudin, S. Auffret, B. Rodmacq, A. Schuhl, *Phys. Rev. Lett.* **2009**, *102*, 137202.
[146] P. P. J. Haazen, E. Murè, J. H. Franken, R. Lavrijsen, H. J. M. Swagten, B. Koopmans, *Nat. Mater.* **2013**, *12*, 299.
[147] H. Yang, A. Thiaville, S. Rohart, A. Fert, M. Chshiev, *Phys. Rev. Lett.* **2015**, *115*, 267210.
[148] C. Moreau-Luchaire, C. Moutafis, N. Reyren, J. Sampaio, C. A. F. Vaz, N. Van Horne, K. Bouzehouane, K. Garcia, C. Deranlot, P. Warnicke, P. Wohlhüter, J.-M. George, M. Weigand, J. Raabe, V. Cros, A. Fert, *Nat. Nanotechnol.* **2016**, *11*, 444.
[149] S. Woo, K. Litzius, B. Krüger, M.-Y. Im, L. Caretta, K. Richter, M. Mann, A. Krone, R. M. Reeve, M. Weigand, P. Agrawal, I. Lemesh, M.-A. Mawass, P. Fischer, M. Kläui, G. S. D. Beach, *Nat. Mater.* **2016**, *15*, 501.
[150] S. Mizukami, E. P. Sajitha, D. Watanabe, F. Wu, T. Miyazaki, H. Naganuma, M. Oogane, Y. Ando, *Appl. Phys. Lett.* **2010**, *96*, 152502.
[151] M. Van Kampen, C. Jozsa, J. T. Kohlhepp, P. LeClair, L. Lagae, W. J. M. De Jonge, B. Koopmans, *Phys. Rev. Lett.* **2002**, *88*, 227201.
[152] A. Ganguly, S. Azzawi, S. Saha, J. A. King, R. M. Rowan-Robinson, A. T. Hindmarch, J. Sinha, D. Atkinson, A. Barman, *Sci. Rep.* **2015**, *5*, 17596.
[153] P. He, X. Ma, J. W. Zhang, H. B. Zhao, G. Lupke, Z. Shi, S. M. Zhou, *Phys. Rev. Lett.* **2013**, *110*, 077203.
[154] H. S. Song, K. D. Lee, J. W. Sohn, S. H. Yang, S. S. P. Parkin, C. Y. You, S. C. Shin, *Appl. Phys. Lett.* **2013**, *103*, 022406.
[155] S. Mizukami, *J. Magn. Soc. Jpn.* **2015**, *39*, 1.
[156] A. J. Schellekens, L. Deen, D. Wang, J. T. Kohlhepp, H. J. M. Swagten, B. Koopmans, *Appl. Phys. Lett.* **2013**, *102*, 082405.
[157] S. Pal, B. Rana, O. Hellwig, T. Thomson, A. Barman, *Appl. Phys. Lett.* **2011**, *98*, 082501.
[158] J. M. Shaw, H. T. Nembach, T. J. Silva, *Appl. Phys. Lett.* **2014**, *105*, 062406.
[159] B. Zhang, A. Cao, J. Qiao, M. Tang, K. Cao, X. Zhao, S. Eimer, Z. Si, N. Lei, Z. Wang, X. Lin, Z. Zhang, M. Wu, W. Zhao, *Appl. Phys. Lett.* **2017**, *110*, 012405.
[160] M. Oogane, T. Kubota, H. Naganuma, Y. Ando, *J. Phys. D: Appl. Phys.* **2015**, *48*, 164012.
[161] V. Kamberský, Czech. *J. Phys., Sect. B* **1976**, *26*, 1366.
[162] A. R. Mackintosh, O. K. Andesen, in *Electrons at the Fermi Surface* (Ed: M. Springford), Cambridge University Press, Cambridge, UK **1980**, p. 149.
[163] G. Kresse, J. Hafner, *Phys. Rev. B* **1993**, *47*, 558.
[164] G. Kresse, J. Furthmüller, *Phys. Rev. B* **1996**, *54*, 11169.
[165] B. Heinrich, D. Fraitová, V. Kamberský, *Phys. Status Solidi* **1967**, *23*, 501.
[166] V. Kamberský, *Can. J. Phys.* **1970**, *48*, 1103.
[167] A. Soumyanarayanan, N. Reyren, A. Fert, C. Panagopoulos, *Nature* **2016**, *539*, 509.
[168] Z. Wang, Z. Li, Y. Liu, S. Li, L. Chang, W. Kang, Y. Zhang, W. Zhao, presented at *2018 IEEE Int. Symp. Circuits and Systems (ISCAS)*, Florence, Italy, May **2018**.
[169] J. Park, G. E. Rowlands, O. J. Lee, D. C. Ralph, R. A. Buhrman, *Appl. Phys. Lett.* **2014**, *105*, 102404.
[170] K. Garello, C. O. Avci, I. M. Miron, M. Baumgartner, A. Ghosh, S. Auffret, O. Boulle, G. Gaudin, P. Gambardella, *Appl. Phys. Lett.* **2014**, *105*, 212402.
[171] C. Zhang, S. Fukami, H. Sato, F. Matsukura, H. Ohno, *Appl. Phys. Lett.* **2015**, *107*, 012401.
[172] S. Mangin, D. Ravelosona, J. A. Katine, M. J. Carey, B. D. Terris, E. E. Fullerton, *Nat. Mater.* **2006**, *5*, 210.
[173] C. Wan, X. Zhang, Z. Yuan, C. Fang, W. Kong, Q. Zhang, H. Wu, U. Khan, X. Han, *Adv. Electron. Mater.* **2017**, *3*, 1600282.
[174] S. Emori, U. Bauer, S. Ahn, E. Martinez, G. S. D. Beach, *Nat. Mater.* **2013**, *12*, 611.
[175] K. Ryu, L. Thomas, S. Yang, S. Parkin, *Nat. Nanotechnol.* **2013**, *8*, 527.
[176] F. Büttner, I. Lemesh, M. Schneider, B. Pfau, C. M. Günther, P. Hessing, J. Geilhufe, L. Caretta, D. Engel, B. Krüger, J. Viefhaus, S. Eisebitt, G. S. D. Beach, *Nat. Nanotechnol.* **2017**, *12*, 1040.
[177] M. I. Dyakonov, V. I. Perel, *Phys. Lett. A* **1971**, *35*, 459.
[178] Y. K. Kato, R. C. Myers, A. C. Gossard, D. D. Awschalom, *Science* **2004**, *306*, 1910.
[179] J. Sinova, S. O. Valenzuela, J. Wunderlich, C. H. Back, T. Jungwirth, *Rev. Mod. Phys.* **2015**, *87*, 1213.
[180] G. Dresselhaus, *Phys. Rev.* **1955**, *100*, 580.
[181] Y. A. Bychkov, E. I. Rashba, *JETP Lett.* **1984**, *39*, 78.
[182] I. M. Miron, T. Moore, H. Szambolics, L. D. Buda-Prejbeanu, S. Auffret, B. Rodmacq, S. Pizzini, J. Vogel, M. Bonfim, A. Schuhl, G. Gaudin, *Nat. Mater.* **2011**, *10*, 419.
[183] L. Liu, O. J. Lee, T. J. Gudmundsen, D. C. Ralph, R. A. Buhrman, *Phys. Rev. Lett.* **2012**, *109*, 096602.
[184] X. Fan, H. Celik, J. Wu, C. Ni, K.-J. Lee, V. O. Lorenz, J. Q. Xiao, *Nat. Commun.* **2014**, *5*, 3042.
[185] K.-W. Kim, S.-M. Seo, J. Ryu, K.-J. Lee, H.-W. Lee, *Phys. Rev. B* **2012**, *85*, 180404.
[186] K.-S. Lee, S.-W. Lee, B.-C. Min, K.-J. Lee, *Appl. Phys. Lett.* **2013**, *102*, 112410.
[187] T. Taniguchi, S. Mitani, M. Hayashi, *Phys. Rev. B* **2015**, *92*, 024428.
[188] M. Wang, W. Cai, D. Zhu, Z. Wang, J. Kan, Z. Zhao, K. Cao, Z. Wang, Y. Zhang, T. Zhang, C. Park, J.-P. Wang, A. Fert, W. Zhao, *Nat. Electron.* **2018**, *1*, 582.
[189] M. Morota, Y. Niimi, K. Ohnishi, D. H. Wei, T. Tanaka, H. Kontani, T. Kimura, Y. Otani, *Phys. Rev. B* **2011**, *83*, 174405.

[190] M. Kazemi, G. E. Rowlands, E. Ipek, R. A. Buhrman, E. G. Friedman, *IEEE Trans. Electron Devices* **2016**, *63*, 848.
[191] E. Sagasta, Y. Omori, S. Vélez, R. Llopis, C. Tollan, A. Chuvilin, L. E. Hueso, M. Gradhand, Y. Otani, F. Casanova, *Phys. Rev. B* **2018**, *98*, 060410.
[192] B. Gu, I. Sugai, T. Ziman, G. Y. Guo, N. Nagaosa, T. Seki, K. Takanashi, S. Maekawa, *Phys. Rev. Lett.* **2010**, *105*, 216401.
[193] P. Laczkowski, Y. Fu, H. Yang, J. C. Rojas-Sánchez, P. Noel, V. T. Pham, G. Zahnd, C. Deranlot, S. Collin, C. Bouard, P. Warin, V. Maurel, M. Chshiev, A. Marty, J. P. Attané, A. Fert, H. Jaffrès, L. Vila, J. M. George, *Phys. Rev. B* **2017**, *96*, 140405.
[194] L. Zhu, D. C. Ralph, R. A. Buhrman, *Phys. Rev. Appl.* **2018**, *10*, 031001.
[195] M. Z. Hasan, C. L. Kane, *Rev. Mod. Phys.* **2010**, *82*, 3045.
[196] Y. Fan, P. Upadhyaya, X. Kou, M. Lang, S. Takei, Z. Wang, J. Tang, L. He, L.-T. Chang, M. Montazeri, G. Yu, W. Jiang, T. Nie, R. N. Schwartz, Y. Tserkovnyak, K. L. Wang, *Nat. Mater.* **2014**, *13*, 699.
[197] Y. Wang, D. Zhu, Y. Wu, Y. Yang, J. Yu, R. Ramaswamy, R. Mishra, S. Shi, M. Elyasi, K. Teo, Y. Wu, H. Yang, *Nat. Commun.* **2017**, *8*, 1364.
[198] J. Han, A. Richardella, S. A. Siddiqui, J. Finley, N. Samarth, L. Liu, *Phys. Rev. Lett.* **2017**, *119*, 077702.
[199] N. H. D. Khang, Y. Ueda, P. N. Hai, *Nat. Mater.* **2018**, *17*, 808.
[200] M. DC, R. Grassi, J.-Y. Chen, M. Jamali, D. R. Hickey, D. Zhang, Z. Zhao, H. Li, P. Quarterman, Y. Lv, M. Li, A. Manchon, K. A. Mkhoyan, T. Low, J.-P. Wang, *Nat. Mater.* **2018**, *17*, 800.
[201] C. O. Avci, K. Garello, M. Gabureac, A. Ghosh, A. Fuhrer, S. F. Alvarado, P. Gambardella, *Phys. Rev. B* **2014**, *90*, 224427.
[202] N. Roschewsky, E. S. Walker, P. Gowtham, S. Muschinske, F. Hellman, S. R. Bank, S. Salahuddin, *Phys. Rev. B* **2019**, *99*, 195103.
[203] J. Qiao, J. Zhou, Z. Yuan, W. Zhao, *Phys. Rev. B* **2018**, *98*, 214402.
[204] J. Yoon, S.-W. Lee, J. H. Kwon, J. M. Lee, J. Son, X. Qiu, K.-J. Lee, H. Yang, *Sci. Adv.* **2017**, *3*, e1603099.
[205] J. M. Lee, J. H. Kwon, R. Ramaswamy, J. Yoon, J. Son, X. Qiu, R. Mishra, S. Srivastava1, K. Cai, H. Yang, *Commun. Phys.* **2018**, *1*, 2.
[206] W. Legrand, R. Ramaswamy, R. Mishra, H. Yang, *Phys. Rev. Appl.* **2015**, *3*, 064012.
[207] W. Fan, J. Zhao, M. Tang, H. Chen, H. Yang, W. Lü, Z. Shi, X. Qiu, *Phys. Rev. Appl.* **2019**, *11*, 034018.
[208] N. Sato, A. El-Ghazaly, R. M. White, S. Wang, *IEEE Trans. Magn.* **2016**, *52*, 1400304.
[209] C. O. Avci, K. Garello, C. Nistor, S. Godey, B. Ballesteros, A. Mugarza, A. Barla, M. Valvidares, E. Pellegrin, A. Ghosh, I. M. Miron, O. Boulle, S. Auffret, G. Gaudin, P. Gambardella, *Phys. Rev. B* **2014**, *89*, 214419.
[210] X. Chen, R. Zarzuela, J. Zhang, C. Song, X. Zhou, G. Shi, F. Li, H. Zhou, W. Jiang, F. Pan, *Phys. Rev. Lett.* **2018**, *120*, 207204.
[211] G. Apachitei, J. J. P. Peters, A. M. Sanchez, D. J. Kim, M. Alexe, *Adv. Electron. Mater.* **2017**, *3*, 1700126.
[212] S. Fukami, C. Zhang, S. DuttaGupta, A. Kurenkov, and H. Ohno, *Nat. Mater.* **2016**, *15*, 535.
[213] W. Zhang, W. Han, S.-H. Yang, Y. Sun, Y. Zhang, B. Yan, S. S. P. Parkin, *Sci. Adv.* **2016**, *2*, e1600759.
[214] S. Peng, X. Li, W. Kang, H. Zhang, L. Wang, Z. Wang, Z. Wang, Y. Zhang, K. L. Wang, W. Zhao, **2018**, arXiv:1804.11025.
[215] S. Nakatsuji, N. Kiyohara, T. Higo, *Nature* **2015**, *527*, 212.
[216] H. Chen, Q. Niu, A. H. MacDonald, *Phys. Rev. Lett.* **2014**, *112*, 017205.
[217] Z. Q. Liu, H. Chen, J. M. Wang, J. H. Liu, K. Wang, Z. X. Feng, H. Yan, X. R. Wang, C. B. Jiang, J. M. D. Coey, A. H. MacDonald, *Nat. Electron.* **2018**, *1*, 172.
[218] C. Sürgers, W. Kittler, T. Wolf, H. V. Löhneysen, *AIP Adv.* **2016**, *6*, 055604.
[219] M. Kimata, H. Chen, K. Kondou, S. Sugimoto, P. K. Muduli, M. Ikhlas, Y. Omori, T. Tomita, A. H. MacDonald, S. Nakatsuji, Y. Otani, *Nature* **2019**, *565*, 627.
[220] P. K. Muduli, T. Higo, T. Nishikawa, D. Qu, H. Isshiki, K. Kondou, D. Nishio-Hamane, S. Nakatsuji, Y. Otani, *Phys. Rev. B* **2019**, *99*, 184425.
[221] Z. Zhao, A. K. Smith, M. Jamali, J.-P. Wang, **2017**, arXiv:1603.09624v2.
[222] S. C. Baek, V. P. Amin, Y.-W. Oh, G. Go, S.-J. Lee, G.-H. Lee, K.-J. Kim, M. D. Stiles, B.-G. Park, K.-J. Lee, *Nat. Mater.* **2018**, *17*, 509.
[223] K. Cai, M. Yang, H. Ju, S. Wang, Y. Ji, B. Li, K. W. Edmonds, Y. Sheng, B. Zhang, N. Zhang, S. Liu, H. Zheng, K. Wang, *Nat. Mater.* **2017**, *13*, 712.
[224] Y.-C. Lau, D. Betto, K. Rode, J. M. D. Coey, P. Stamenov, *Nat. Nanotechnol.* **2016**, *11*, 758.
[225] X. Wang, C. Wan, W. Kong, X. Zhang, Y. Xing, C. Fang, B. Tao, W. Yang, L. Huang, H. Wu, M. Irfan, X. Han, *Adv. Mater.* **2018**, *30*, 1801318.
[226] G. Yu, P. Upadhyaya, Y. Fan, J. G. Alzate, W. Jiang, K. L. Wong, S. Takei, S. A. Bender, L. Chang, Y. Jiang, M. Lang, J. Tang, Y. Wang, Y. Tserkovnyak, P. K. Amiri, K. L. Wang, *Nat. Nanotechnol.* **2014**, *9*, 548.
[227] Q. Ma, Y. Li, D. B. Gopman, Y. P. Kabanov, R. D. Shull, C. L. Chien, *Phys. Rev. Lett.* **2018**, *120*, 117703.
[228] L. You, O. Lee, D. Bhowmik, D. Labanowski, J. Hong, J. Bokor, S. Salahuddina, *Proc. Natl. Acad. Sci. USA* **2015**, *112*, 10310.
[229] V. P. Amin, J. Zemen, M. D. Stiles, *Phys. Rev. Lett.* **2018**, *121*, 136805.
[230] A. van den Brink, S. Cosemans, S. Cornelissen, M. Manfrini, A. Vaysset, W. Van Roy, T. Min, H. J. M. Swagten, B. Koopmans, *Appl. Phys. Lett.* **2014**, *104*, 012403.
[231] N. Sato, F. Xue, R. M. White, C. Bi, S. Wang, *Nat. Electron.* **2018**, *1*, 508.
[232] M. Kazemi, G. E. Rowlands, S. Shi, R. A. Buhrman, E. G. Friedman, *IEEE Trans. Electron Devices* **2016**, *63*, 4499.
[233] I. Dzyaloshinskii, *J. Phys. Chem. Solids* **1958**, *4*, 241.
[234] T. Moriya, *Phys. Rev.* **1960**, *120*, 91.
[235] S. Muhlbauer, B. Binz, C. Pfleiderer, A. Rosch, A. Neubauer, R. Georgii, P. Boni, *Science* **2013**, *323*, 915.
[236] H. Du, R. Che, L. Kong, X. Zhao, C. Jin, C. Wang, J. Yang, W. Ning, R. Li, C. Jin, X. Chen, J. Zang, Y. Zhang, M. Tian, *Nat. Commun.* **2015**, *6*, 8504.
[237] D. A. Gilbert, B. B. Maranville, A. L. Balk, B. J. Kirby, P. Fischer, D. T. Pierce, J. Unguris, J. A. Borchers, K. Liu, *Nat. Commun.* **2015**, *6*, 8462.
[238] G. Yu, P. Upadhyaya, K. L. Wong, W. Jiang, J. G. Alzate, J. Tang, P. K. Amiri, K. L. Wang, *Phys. Rev. B* **2014**, *89*, 104421.
[239] D. A. Allwood, G. Xiong, C. C. Faulkner, D. Atkinson, D. Petit, R. P. Cowburn, *Science* **2005**, *309*, 1688.
[240] S. Zhang, Z. Li, *Phys. Rev. Lett.* **2004**, *93*, 127204.
[241] A. Fert, N. Reyren, V. Cros, *Nat. Rev. Mater.* **2017**, *2*, 17031.
[242] A. Thiaville, S. Rohart, E. Jue, V. Cros, A. Fert, *Europhys. Lett.* **2012**, *100*, 57002.
[243] J. Sampaio, V. Cros, S. Rohart, A. Thiaville, A. Fert, *Nat. Nanotechnol.* **2013**, *8*, 839.
[244] W. Jiang, X. Zhang, G. Yu, W. Zhang, X. Wang, M. B. Jungfleisch, J. E. Pearson, X. Cheng, O. Heinonen, K. L. Wang, Y. Zhou, A. Hoffmann, S. G. E. te Velthuis, *Nat. Phys.* **2017**, *13*, 162.
[245] A. Hrabec, J. Sampaio, M. Belmeguenai, I. Gross, R. Weil, S. M. Cherif, A. Stashkevich, V. Jacques, A. Thiaville, S. Rohart, *Nat. Commun.* **2017**, *8*, 15765.

[246] X. Zhang, Y. Zhou, M. Ezawa, *Nat. Commun.* **2016**, *7*, 10293.
[247] X. Zhang, J. Xia, Y. Zhou, D. Wang, X. Liu, W. Zhao, M. Ezawa, *Phys. Rev. B* **2012**, *94*, 094420.
[248] H. Yang, O. Boulle, V. Cros, A. Fert, M. Chshiev, *Sci. Rep.* **2018**, *8*, 12356.
[249] D. Cortés-Ortuño, P. Landeros, *J. Phys.: Condens. Matter* **2013**, *25*, 156001.
[250] J. H. Moon, S. M. Seo, K. J. Lee, K. W. Kim, J. Ryu, H. W. Lee, R. D. McMichael, M. D. Stiles, *Phys. Rev. B* **2013**, *88*, 184404.
[251] K. Di, V. L. Zhang, H. S. Lim, S. C. Ng, M. H. Kuok, J. Yu, J. Yoon, X. Qiu, H. Yang, *Phys. Rev. Lett.* **2015**, *114*, 047201.
[252] A. Hrabec, M. Belmeguenai, A. Stashkevich, S. M. Chérif, S. Rohart, Y. Roussigné, A. Thiaville, *Appl. Phys. Lett.* **2017**, *110*, 242402.
[253] J. M. Lee, C. Jang, B. C. Min, S. W. Lee, K. J. Lee, J. Chang, *Nano Lett.* **2016**, *16*, 62.
[254] K. Zakeri, Y. Zhang, J. Prokop, T. H. Chuang, N. Sakr, W. X. Tang, J. Kirschner, *Phys. Rev. Lett.* **2010**, *104*, 137203.
[255] M. Mena, R. S. Perry, T. G. Perring, M. D. Le, S. Guerrero, M. Storni, D. T. Adroja, C. Rüegg, D. F. McMorrow, *Phys. Rev. Lett.* **2014**, *113*, 047202.
[256] F. Garcia-Sanchez, P. Borys, A. Vansteenkiste, J.-V. Kim, R. L. Stamps, *Phys. Rev. B* **2014**, *89*, 224408.
[257] S. G. Je, D. H. Kim, S. C. Yoo, B. C. Min, K. J. Lee, S. B. Choe, *Phys. Rev. B* **2013**, *88*, 214401.
[258] A. Cao, X. Zhang, B. Koopmans, S. Peng, Y. Zhang, Z. Wang, S. Yan, H. Yang, W. Zhao, *Nanoscale* **2018**, *10*, 12062.
[259] M. Vanatka, J.-C. Rojas-Sanchez, J. Vogel, M. Bonfim, A. Thiaville, S. Pizzini, *J. Phys. Condens. Matter* **2015**, *27*, 326002.
[260] D. S. Han, N. H. Kim, J. S. Kim, Y. Yin, J. W. Koo, J. Cho, S. Lee, M. Kläui, H. J. M. Swagten, B. Koopmans, C. Y. You, *Nano Lett.* **2016**, *16*, 4438.
[261] C. F. Pai, M. Mann, A. J. Tan, G. S. D. Beach, *Phys. Rev. B* **2016**, *93*, 144409.
[262] A. Hrabec, N. A. Porter, A. Wells, M. J. Benitez, G. Burnell, S. McVitie, D. McGrouther, T. A. Moore, C. H. Marrows, *Phys. Rev. B* **2019**, *99*, 020402(R).
[263] K. Shahbazi, J.-V. Kim, H. T. Nembach, J. M. Shaw, A. Bischof, M. D. Rossell, V. Jeudy, T. A. Moore, C. H. Marrows, *Phys. Rev. B* **2014**, *90*, 094409.
[264] S. Jaiswal, K. Litzius, I. Lemesh, F. Büttner, S. Finizio, J. Raabe, M. Weigand, K. Lee, J. Langer, B. Ocker, G. Jakob, G. S. D. Beach, M. Kläui, *Appl. Phys. Lett.* **2017**, *111*, 022409.
[265] A. Belabbes, G. Bihlmayer, S. Blügel, A. Manchon, *Sci. Rep.* **2016**, *6*, 24634.
[266] O. Boulle, J. Vogel, H. Yang, S. Pizzini, D. de S. Chaves, A. Locatelli, T. O. Menteş, A. Sala, L. D. Buda-Prejbeanu, O. Klein, M. Belmeguenai, Y. Roussigné, A. Stashkevich, S. M. Chérif, L. Aballe, M. Foerster, M. Chshiev, S. Auffret, I. M. Miron, G. Gaudin, *Nat. Nanotechnol.* **2016**, *11*, 449.
[267] R. Lo Conte, E. Martinez, A. Hrabec, A. Lamperti, T. Schulz, L. Nasi, L. Lazzarini, R. Mantovan, F. Maccherozzi, S. S. Dhesi, B. Ocker, C. H. Marrows, T. A. Moore, M. Kläui, *Phys. Rev. B* **2015**, *91*, 014433.
[268] I. Gross, L. J. Martínez, J.-P. Tetienne, T. Hingant, J.-F. Roch, K. Garcia, R. Soucaille, J. P. Adam, J.-V. Kim, S. Rohart, A. Thiaville, J. Torrejon, M. Hayashi, V. Jacques, *Phys. Rev. B* **2016**, *94*, 064413.
[269] R. A. Khan, P. M. Shepley, A. Hrabec, A. W. J. Wells, B. Ocker, C. H. Marrows, T. A. Moore, *Appl. Phys. Lett.* **2016**, *109*, 132404.
[270] C. Park, J. J. Kan, C. Ching, J. Ahn, L. Xue, R. Wang, A. Kontos, S. Liang, M. Bangar, H. Chen, S. Hassan, M. Gottwald, X. Zhu, M. Pakala, S. H. Kang, *IEEE Int. Electron Devices Meet.* **2015**, *26*, 2.
[271] S. Chung, T. Kishi, J. W. Park, M. Yoshikawa, K. S. Park, T. Nagase, K. Sunouchi, H. Kanaya, G. C. Kim, *IEEE Int. Electron Devices Meet.* **2016**, *27*, 1.
[272] B. Balke, G. H. Fecher, J. Winterlik, C. Felser, *Appl. Phys. Lett.* **2007**, *90*, 152504.
[273] K. Watanabe, B. Jinnai, S. Fukami, H. Sato, H. Ohno, *Nat. Commun.* **2018**, *9*, 663.
[274] N. Perrissin, S. Lequeux, N. Strelkov, L. Vila, L. Buda-Prejbeanu, S. Auffret, R. C. Sousa, I. L. Prejbeanu, B. Dieny, *Nanoscale* **2018**, *10*, 12187.
[275] Y. Zhang, X. Lin, J. P. Adam, G. Agnus, W. Kang, W. Cai, J. R. Coudevylle, N. Isac, J. Yang, H. Yang, K. Cao, H. Cui, D. Zhang, Y. Zhang, C. Zhao, W. Zhao, D. Ravelosona, *Adv. Electron. Mater.* **2018**, *4*, 1700461.
[276] B. Yang, L. Tao, L. Jiang, W. Chen, P. Tang, Y. Yan, X. Han, *Phys. Rev. Appl.* **2018**, *9*, 54019.
[277] L. Pan, L. Huang, M. Zhong, X.-W. Jiang, H. Deng, J. Li, J. Xia, Z. Wei, *Nanoscale* **2018**, *10*, 22196.
[278] J. Zhang, X. Z. Chen, C. Song, J. F. Feng, H. X. Wei, J. T. Lü, *Phys. Rev. Appl.* **2018**, *9*, 44034.
[279] W. Kang, Y. Ran, W. Lv, Y. Zhang, W. Zhao, *IEEE Magn. Lett.* **2016**, *7*, 3106205.
[280] H. Yoda, N. Shimomura, Y. Ohsawa, S. Shirotori, Y. Kato, T. Inokuchi, Y. Kamiguchi, B. Altansargai, Y. Saito, K. Koi, H. Sugiyama, S. Oikawa, M. Shimizu, M. Ishikawa, K. Ikegami, A. Kurobe, A. H. Density, *IEEE Int. Electron Devices Meet.* **2016**, *27*, 6.
[281] H. Lee, A. Lee, F. Ebrahimi, P. K. Amiri, K. L. Wang, *IEEE Electron Device Lett.* **2017**, *38*, 1343.
[282] Y. Yan, C. Wan, X. Zhou, G. Shi, B. Cui, J. Han, Y. Fan, X. Han, K. L. Wang, F. Pan, C. Song, *Adv. Electron. Mater.* **2016**, *2*, 1600219.
[283] L. Baldrati, C. Rinaldi, A. Manuzzi, M. Asa, L. Aballe, M. Foerster, N. Biškup, M. Varela, M. Cantoni, R. Bertacco, *Adv. Electron. Mater.* **2016**, *2*, 1600085.

